High Performance FeNC and Mn-oxide/FeNC Layers for AEMFC Cathodes

Pietro Giovanni Santori, Florian Dominik Speck, Serhiy Cherevko, Horie Adabi Firouzjaie, Xiong Peng, William Mustain, Frédéric Jaouen

High performance FeNC and Mn-oxide/FeNC layers for AEMFC cathodes

Pietro Giovanni Santori,[1] Florian Dominik Speck,[2,3] Serhiy Cherevko,[2] Horie Adabi Firouzjaie,[4] Xiong Peng,[4] William E. Mustain,[4] Frédéric Jaouen[1]

1. ICGM, Univ. Montpellier, CNRS, ENSCM, Montpellier, France
2. Helmholtz-Institute Erlangen-Nürnberg for Renewable Energy (IEK-11), Forschungszentrum Jülich, Egerlandstr. 3, 91058 Erlangen, Germany
3. Department of Chemical and Biological Engineering, Friedrich-Alexander-Universität Erlangen-Nürnberg, 91058 Erlangen, Germany
4. Department of Chemical Engineering, University of South Carolina, Columbia, SC 29208, USA

To whom correspondence should be addressed:

F. Jaouen; frederic.jaouen@umontpellier.fr

W. Mustain; MUSTAINW@mailbox.sc.edu

Abstract

While the Anion Exchange Membrane Fuel Cell (AEMFC) is gaining interest due to high power performance recently achieved with platinum-group-metal (PGM) catalysts, its implementation will require high-performing PGM-free cathodes. FeNC catalysts have shown high activity and stability for the Oxygen Reduction Reaction (ORR) in alkaline electrolyte; however, the production of hydrogen peroxide during ORR can lead to premature degradation of FeNC and ionomer. In order to minimize the amount of peroxide formed on FeNC, α-MnO_2, β-MnO_2, δ-MnO_2 and α-Mn_2O_3 were investigated as co-catalysts, with the aim of increasing the apparent activity of FeNC-based cathodes for the hydrogen peroxide reduction reaction (HPRR). The specific activity of α-Mn_2O_3 for the HPRR was distinctly superior to the other Mn-oxides. The four Mn-oxides were mixed with a FeNC catalyst comprising atomically-dispersed FeN_x sites, showing higher HPRR activity and higher four-electron ORR selectivity than FeNC alone. The stability of α-Mn_2O_3/FeNC was studied *operando* by on-line inductively-coupled plasma mass spectrometry, to evaluate the potential and time dependent leaching of Mn and Fe. Finally, FeNC and α-Mn_2O_3/FeNC were applied at the cathode of AEMFCs, both achieving similar or higher current density at 0.9 V than a Pt/C commercial cathode, and peak power densities of *ca* 1 $W \cdot cm^{-2}$.

Introduction

The energy-environment nexus calls for the development of renewable energy sources and more efficient machines. Renewable electric power, produced from solar or wind energies for example, can be efficiently converted to hydrogen *via* water electrolysis, and hydrogen used as a green fuel, on demand.[1] To this end, fuel cell devices can efficiently re-convert renewable H_2 and O_2 from air to electric power with high efficiency. This technology is well positioned to compete, among other applications, with internal combustion engines for automotive application.[2] Among different types of fuel cells, Proton Exchange Membrane Fuel Cells (PEMFCs) are currently the ones envisioned and developed by the automotive industry for transportation application, due to their high power density, low internal resistance, low maintenance, long-term durability and fast start-up.[3,4] In the long term, however, the main drawback of PEMFCs is tied to the kinetics of the Oxygen Reduction Reaction (ORR) that occurs at the cathode side. The sluggishness of the ORR in the acidic PEMFC forces the use of platinum-based catalysts to minimize the losses in energy efficiency and power density that are associated with the ORR overpotential.[5,6] Platinum is a rare and expensive metal that increases the production cost of the device, threatening the large-scale commercialization of PEMFCs and its sustainability.[5-8] The need to reduce the amount of platinum (at large, platinum group metals (PGMs), Pt and Pd being the least rare PGMs) in high-performance PEMFCs has led the scientific community involved in electrocatalysis to investigate two separate approaches, one leaning on the improvement of PGM (mostly Pt) catalysts and cathode layers to utilize more efficiently such metals,[9-14] and another exploring the synthesis of PGM-free catalysts with activity and durability that must, ultimately, become comparable to those of Pt-based catalysts.

Among the PGM-free catalysts investigated since the early 2000's, a class of MNC catalysts with 3d transition metals (M=Fe and Co, in particular) integrated in a N-doped carbon matrix has hitherto shown the most promising activity and stability in acidic media,[15-21] though oxynitrides of transition metals of group 4 and 5 in the periodic table have also been reported with promising activity.[22-24] The nature of the most active catalytic sites in MNC catalysts obtained *via* pyrolysis

has been controversial since their emergence. However, recent studies from several groups are now converging to the same conclusion that, in acidic medium, the most active and stable sites in MNC catalysts are atomically-dispersed MN_x moieties.[25-34] This conclusion could be reached with the preparation of model MNC materials, exclusively comprising single-metal-atom structures and no metal clusters (to the detection limit of X-ray absorption and ^{57}Fe Mössbauer spectroscopies as well as scanning transmission electron microscopy). Combined theoretical and experimental interpretation of the spectroscopic response of such model MNC catalysts prepared from different precursors are also converging to the picture of FeN_x and CoN_x moieties ($x \leq 4$) embedded in the carbon matrix as porphyrinic MN_4C_{12} or pyridinic MN_4C_{10} structures, with the transition metal in a +II or +III oxidation state and in different spin states.[17,26,27,35-38] Binuclear Fe_2N_5 sites have also been proposed and could be a minority site in FeNC catalysts, but possibly with higher turnover frequency.[39]

Besides the need to further improve the activity of MNC catalysts for matching the high PEMFC performance currently obtained with Pt-based catalysts, the main bottleneck for the industrial application of MNC catalysts in PEMFC is presently their limited durability during PEMFC operation. Their degradation mechanisms have been intensively explored in rotating disk electrode (RDE), PEMFC and *ex situ* with non-electrochemical Fenton tests.[19,34,40-50] While some MNC catalysts have shown high stability when load-cycled in deaerated acidic electrolytes,[34,42] similar load-cycling O_2-saturated electrolytes has resulted in irreversible ORR activity loss, assigned to reactive oxygen species formed during ORR, such as hydrogen peroxide, triggering unexpected carbon corrosion at such low potential and the transformation of FeN_x sites to iron oxide.[51] All MNC catalysts can also be expected to suffer from carbon corrosion during startup/shutdown accelerated stress tests, leading to the destruction of MN_x sites and the leaching of the metal cations.[34,52] Such transient events can be mitigated at system level and are therefore less critical than the degradation occurring during normal PEMFC cathode operation.

Highly microporous FeNC catalysts, often prepared *via* NH_3 pyrolysis, are the most active MNC catalysts in acidic media, but they are also the least stable in operating PEMFCs.[16,18,40,53,54] Recent studies by Dodelet's group and also our group have shown that NH_3-pyrolyzed microporous FeNC materials show distinctly faster Fe leaching rates in acidic medium than FeNC catalysts similarly prepared but pyrolyzed in inert gas.[43,55] Our study reported that the leaching rate of iron in O_2-saturated acid electrolyte during a linear scan between 1 and 0 V vs. RHE was *circa* 10 times higher for a microporous FeNC catalyst (prepared via a first pyrolysis in Ar and a second pyrolysis in ammonia, labelled $Fe_{0.5}$-NH_3) relative to the FeNC catalyst prepared identically except that it was not subjected to the second pyrolysis in ammonia (labelled $Fe_{0.5}$-Ar).[43] Furthermore, the online and *operando* measurement identified that the Fe leaching rate increased when the potential was decreased from 1 to 0 V *vs*. RHE, with an onset potential at *ca* 0.75 V *vs.* RHE and a peak of dissolution rate at 0.2-0.3 V *vs.* RHE. It was also shown that both the $Fe_{0.5}$-NH_3 and $Fe_{0.5}$-Ar catalysts are exclusively comprised of FeN_x sites. Thus, the distinctly lower stability of FeN_x sites in $Fe_{0.5}$-NH_3 in acidic electrolyte could be assigned to either the higher microporosity of $Fe_{0.5}$-NH_3, or to weaker Fe-N bonds in acidic medium. These new insights must also be connected with previous studies from Dodelet's group where it was shown that NH_3 pyrolysis results in nitrogen-groups with high pKa values, and the high initial activity in acid medium was proposed to be due to the protonation of such N-groups in acidic medium, and their fast deactivation due to subsequent anion adsorption on positively-charged NH groups.[56] Combined together, those results can be interpreted as the coordination of Fe cations with highly basic N-ligands in $Fe_{0.5}$-NH_3, with the Metal-N coordination leading to high ORR activity but low stability in acid media due to the competition between Fe cations and protons for such highly basic N-groups. Strongly supporting this hypothesis, $Fe_{0.5}$-NH_3 was as stable as $Fe_{0.5}$-Ar in alkaline electrolyte, both from the perspective of the *operando*-measured Fe leaching rate in O_2-saturated electrolyte and from the measured ORR activity before and after 5,000 load cycles.[43] The mass activity of $Fe_{0.5}$-NH_3 at 0.9 V *vs.* RHE in 0.1 M KOH was 4.6 $A \cdot g^{-1}$, among the highest reported mass activities for MNC catalysts thus far.[57-60]

The high activity combined with high stability in alkaline medium of the most active FeNC catalysts prepared *via* ammonia pyrolysis is thus promising for their application in Anion Exchange Membrane Fuel Cells (AEMFCs). AEMFCs have recently received significant attention as a possibly much lower cost alternative to PEMFCs,[61-66] particularly since the emergence of very high performing and stable cells over the past two years.[67-71] However, essentially all modern AEMFCs are operated with PGM-based catalysts despite the fact that the highly touted low cost of future AEMFCs relies on the development of highly active and stable PGM-free catalysts for both the cathode and anode. At the cathode, production of hydrogen peroxide during AEMFC operation on FeN_4 sites or on the N-doped carbon surface might limit device lifetime.[72,73] Hydrogen peroxide, a reaction intermediate produced by the $2+2e^-$ ORR pathway, is a strong oxidizer, which, at low pH and, in the presence of 3d transition metal cations, undergoes Fenton's reaction, producing reactive oxygen species (ROS) such as ·OH and ·OOH.[45,74] In high-pH environment, rather than ·OH and ·OOH, it is the superoxide radical ($O_2^{\cdot-}$) that is expected from Fenton reactions between hydrogen peroxide and 3d metal cations, or as an ORR intermediate. The superoxide radical has recently been shown to be positively correlated with the decrease in ion-exchange capacity and conductivity of AEMs in an operating AEMFC with *in situ* fluorescence spectroscopy.[72,73] In contrast, Fenton reactions between FeNC catalysts and hydrogen peroxide have recently been shown to lead to strong ORR deactivation when occurring in acid electrolyte, but to no ORR deactivation when occurring in alkaline electrolyte.[45] Nevertheless, HO_2^- might strongly bind on the Fe-based active sites and, if not electro-reduced to water sufficiently quickly, might poison the FeN_4 active sites. This effect would be exacerbated in the confined environment of micropores, where both the O_2 access and removal of formed peroxide are limited.[45] The formation of hydrogen peroxide from $2e^-$ ORR is also unwanted in AEMFCs because it lowers the achievable efficiency and power density.

For those reasons, the aim of this work is to identify a stable and active PGM-free electrocatalyst for the $2e^-$ reduction of HO_2^- to OH^- in alkaline electrolyte, and to study such a catalyst in combination with the highly active and stable $Fe_{0.5}$-NH_3 catalyst mentioned previously.

With such a composite catalyst, we aim to decrease the amount of peroxide produced during ORR in alkaline electrolyte below the level observed on $Fe_{0.5}$-NH_3. It is important to remind here that, in contrast to the case in acidic medium, the ORR activity of metal-free N-doped carbons in alkaline medium is not negligible.[75-77] Thus, metal-free nitrogen functional groups can significantly contribute to the ORR in parallel with FeN_x sites, in any FeNC catalyst. Such metal-free N-groups typically catalyse the 2e- ORR to HO_2^-. The role of a co-catalyst that is selected for its high activity toward hydrogen peroxide reduction reaction (HPRR) is thus to scavenge hydrogen peroxide produced either at FeN_x or metal-free N-sites, in alkaline electrolyte. Manganese oxides have been well-known for decades for their high heterogeneous catalytic activity toward H_2O_2 disproportionation, which has been investigated in particular for propulsion of space and undersea vehicles.[78,79] Surprisingly, however, while various transition-metal-oxides have previously been shown to work in tandem with carbon catalysts (carbon catalysing O_2 electro-reduction to HO_2^- and metal-oxides catalysing the HPRR),[80-82] the investigation of the specific HPRR activity of different Mn-oxide polymorphs has only recently been investigated by Ryabova *et al.*[83,84] Among the different Mn-oxide polymorphs that were investigated (α-Mn_2O_3, $LaMnO_3$, β-MnO_2, α-MnOOH and Mn_3O_4), α-Mn_2O_3 was identified as the initially most active one, followed by β-MnO_2. Structure-Activity correlations were established, identifying the Mn^{IV}/Mn^{III} redox potential as a key descriptor to predict the onset potential for HPRR.

From these previous works, we selected four Mn-oxide polymorphs, *i.e.* three allotropes of MnO_2, namely α-MnO_2, β-MnO_2 and δ-MnO_2, and one Mn-oxide with a different stoichiometry, *i.e.* Mn_2O_3, which showed to be the most active for HPRR in Ref. [83]. The stability of the same four MnO_x materials was recently investigated by us in a parallel work using a scanning flow cell coupled to inductively coupled mass spectroscopy (SFC/ICP-MS).[85] That work evidenced higher leaching rates of manganese during electrochemical load-cycling conditions in O_2-saturated 0.1 M NaOH electrolyte than in N_2-saturated electrolyte. By following the Mn leaching rate upon controlled addition of hydrogen peroxide in the electrolyte, we could demonstrate that the increased

Mn leaching during ORR is triggered by hydrogen peroxide produced during the ORR. We also evidenced that α-Mn_2O_3 was the most stable Mn-oxide in this series in the ORR potential range, with lowest dissolution rate of manganese.

The objective of the present work is to investigate the HPRR activity in alkaline electrolyte of α-MnO_2, β-MnO_2, δ-MnO_2, and α-Mn_2O_3, and to investigate the effect of the Mn-oxides on the ORR activity, selectivity and HPRR activity of composite catalysts prepared from a mix of $Fe_{0.5}$-NH_3 and each one of these oxides. The HPRR activity was studied in a RDE setup while the ORR activity and selectivity were measured with a Rotating Ring Disk Electrode (RRDE) setup. The activity and performance of both $Fe_{0.5}$-NH_3 and α-Mn_2O_3/ $Fe_{0.5}$-NH_3 cathodes were also investigated in operating AEMFCs.

Experimental

Synthesis of manganese oxides

The synthesis of pure α–, β–, δ–MnO_2 and α–Mn_2O_3 phases was performed according to literature reports, and as detailed in our recent study.[85] A brief description is given here for each phase. The α–MnO_2 phase was obtained by reducing $KMnO_4$ in ultrapure water (18 MΩ) and fumaric acid at room temperature. The resulting gel was filtered, washed with ultrapure water and dried.[25] δ–MnO_2 was obtained via the reduction of $KMnO_4$ in a mixture of water, H_2SO_4 and ethanol, also at room temperature.[86] To obtain β–MnO_2, the dried δ–MnO_2 powder was calcined at 450 °C. For preparing α–Mn_2O_3, γ-MnOOH was prepared in a first step, and then calcined at 550°C for 12 h.[87] For the first step, γ-MnOOH was synthesized dissolving $Mn(CH_3COO)_2{\cdot}4H_2O$ and $KMnO_4$ in deionized water, the solution refluxed for 12 h and then washed with water and dried.[88]

Synthesis of $Fe_{0.5}$-NH_3

$Fe_{0.5}$-NH_3 was prepared *via* the sacrificial metal-organic framework method.[43] Commercial ZIF-8 (Basolite® Z1200, Sigma Aldrich), 1,10-phenantroline (≥ 99%, Sigma Aldrich) and iron (II) acetate (≥99.99%, Sigma Aldrich) were mixed in weight ratios of 4/1 for ZIF-8/phenanthroline and 0.5 wt% of iron in the complete catalyst precursor, using planetary ball milling (400 rpm, four cycles of 30 minutes milling with 5 minutes pause between each cycle). The catalyst precursor powder was then collected from the jar, transferred in a quartz boat and inserted in a quartz tube. For the first pyrolysis, the oven was pre-equilibrated at 1050°C for 2 h while a continuous flow of Ar passed through the tube, with the quartz boat and catalyst precursor inside the tube but outside the heating zone. After 2 h, the quartz boat was pushed in the heating zone in three steps of 30 seconds ("flash pyrolysis"), with the help of an outer magnet and a quartz rod with magnet attached at one end, located inside the tube. The catalyst precursor was pyrolysed in Ar at 1050°C for exactly 1 h, then the split-hinge oven opened and the tube removed and let to cooldown for 20 min, still

under Ar flow. A second pyrolysis was then performed, following the above-mentioned procedure, but using pure NH_3 instead of Ar, an oven temperature of 950°C and a pyrolysis duration of 5 min. The final product is collected directly from the quartz boat ($Fe_{0.5}$-NH_3).

Preparation of MnO_x/Vulcan and MnO_x/$Fe_{0.5}$-NH_3 composites

Each Mn-oxide phase was mixed with Vulcan carbon black in a weight ratio of 1/4 by manual grinding. The Mn-oxides were mixed with $Fe_{0.5}$-NH_3 with the same procedure and weight ratio.

Physical and morphological characterization

The crystalline structure of the four manganese oxides was verified using X-ray Powder Diffraction (XRPD) with PANAlytical X'pert diffractometer in Bragg-Brentano configuration, using a CuK_α source (λ=1.5406 Å) in a 2θ range of 5-80° with a step size of 0.035°. The most intense peaks were compared to the literature using PANalytical X'Pert Highscore Plus (version 3.0e). To analyse the morphology of the Mn-oxides, $Fe_{0.5}$-NH_3 and α-Mn_2O_3/$Fe_{0.5}$-NH_3, scanning electron microscopy (SEM) was applied (Hitachi S4800). Specific surface area of the four Mn-oxides was determined using the Brunauer–Emmett–Teller (BET) method, cleaning previously the sample with flowing nitrogen at 200°C for 5 h and then measuring the sorption of nitrogen at 77 K (Micromeritics ASAP 2020). Elemental distribution in the α-Mn_2O_3/$Fe_{0.5}$-NH_3 composite was analysed with SEM (ZEISS EVO HD15) coupled with Energy-dispersive X-ray spectroscopy (EDX, Oxford Instruments X-Max ^{N} SDD Detector).

Electrochemical characterization

The ORR activity and HO_2^- production during ORR were measured with a RRDE setup (Pine Instruments) in 0.1 M KOH, using a three-electrode configuration. The reference electrode was a Pt-wire immersed in a H_2-saturated electrolyte separated from the main compartment by a

fritted glass, acting as a reversible hydrogen electrode (RHE). The counter electrode was a graphite rod immersed in the electrolyte, at a fixed distance from the working electrode. The latter was a glassy carbon tip (5.6 mm of diameter) where the catalyst is deposited. The peroxide produced at the working electrode was detected at the Pt ring. The HPRR activity was measured in a RDE setup (Pine instruments) in the same conditions (glassy carbon tip of 5 mm diameter). The inks were prepared adding in sequence 54 µL of Nafion® (5% perfluorinated resin solution), 744 µL of ethanol and 92 µL of ultrapure water to 5 mg of FeNC, 20%-MnO_x/C or 20%-MnO_x/FeNC. The mixture was then sonicated for 1 h for homogenization. Then, 8.8 µL of the dispersion was deposited on the RRDE-GC tip, while 7 µL are drop cast on RDE-GC tip, and dried in air at room temperature, to obtain a total catalyst loading of 0.2 $mg \cdot cm^{-2}$. For measuring the ORR activity of the Vulcan carbon black (used for Mn-oxides), an aliquot of 7.0 µL was drop cast on the RRDE-tip and 5.6 µL on the RDE-tip, in order to reach a loading of 0.16 mg cm^{-2}. This corresponds to the loading of Vulcan in the active layers of 20%-MnO_x/C. The electrochemical surface area of the Mn-oxides was assessed on 20%-MnO_x/C composite layers in N_2-saturated electrolyte by cycling at 10 $mV \cdot s^{-1}$ and under 1600 rpm rotation the potential between 0.45 and 1 V *vs.* RHE (SP-300, BioLogic Potentiostat). The lower range potential of 0.45 V was chosen to minimize Mn leaching.[85] To measure the ORR activity and selectivity, the solution was saturated with O_2 and the potential scanned in the range 0 - 1 V *vs*. RHE with a scan rate of 1 mV s^{-1}, while the potential of 1.2 V *vs.* RHE was applied to the Pt ring. To measure the activity toward HPRR, a RDE configuration was used, and the measurement performed in N_2-saturated 0.1 M KOH with 2 mM H_2O_2, scanning the potential at 1 $mV \cdot s^{-1}$ in the range 0.45 – 1.0 V vs. RHE. During ORR and HPRR measurements, the scan rate of 1 $mV \cdot s^{-1}$ was sufficiently low to neglect non-Faradaic currents.

Operando Scanning Flow Cell – Inductively Coupled Plasma Mass Spectroscopy

To evaluate the stability of the α-Mn_2O_3/$Fe_{0.5}$-NH_3 catalyst, a custom made polycarbonate SFC coupled with ICP-MS (Perkin Elmer, NexION 350X) is used to measure *in situ* the dissolution

of manganese and iron during electrochemical protocols. Electrochemical measurements have been carried out in a three electrode configuration using a graphite counter electrode, Ag/AgCl reference electrode (Metrohm) and glassy carbon as working electrode. Electrochemistry is applied with a Potentiostat (Gamry, Reference 600) in 0.05 M NaOH (Merck, Certipur), reaching a controlled pH (Mettler Toledo, SevenExcellence) of 12.7, used to convert the potentials of the Ag/AgCl to the RHE.

AEMFC testing

The catalytic inks were prepared following the procedure described in Omasta *et al.*, manually grinding the catalyst and ETFE (ethylene tetrafluoroethylene) powder ionomer[89], and then dispersing the solids in a mixed solvent of H_2O and 1-propanol (10 vol % H_2O). All anodes were prepared from a 60% PtRu/C commercial catalyst (Johnson Matthey, 2:1 Pt:Ru mass ratio), mixed with Vulcan to reach 40 wt% PtRu/C. 150 mg of 40 wt% PtRu/C and 37.53 mg of ETFE were weighed to prepare the anode ink (ionomer/carbon ratio 0.41). Pt/C cathodes were prepared from a 60 wt% Pt/C commercial catalyst (Johnson Matthey) mixed with Vulcan to reach 40 wt% Pt/C. The catalyst and AEI mass were the same as used for the anode ink. For $Fe_{0.5}$-NH_3 cathodes, 82.59 mg of catalyst was mixed with 17.35 mg ETFE AEI (ionomer/carbon ratio 0.21). For α-Mn_2O_3/ $Fe_{0.5}$-NH_3 cathodes, 20.91 mg α-Mn_2O_3, 82.59 mg $Fe_{0.5}$-NH_3 and 17.35 mg ETFE were mixed together. The dispersion was then sonicated in an ice bath for 1 h and then sprayed on a gas diffusion layer (Toray 60, 5 wt % PTFE wet-proofing) using an airbrush (Iwata Eclipse HP CS). The obtained gas diffusion electrodes and ETFE membrane (50 µm thick in fully swollen conditions) were then soaked for 20 min in 1 M KOH, and this was repeated two times. The electrodes and membrane were combined to create Membrane Electrode Assemblies (MEAs) without prior hot-pressing in single-cell Scribner fuel cell hardware using Teflon gaskets, with the gasket thickness chosen to reach 25% compression. The AEMFC was operated using a Scribner 850e Fuel cell test system, flowing H_2/O_2 at 1.0 L min^{-1} with a cell temperature of 60°C. No back pressure was applied on

anode and cathode sides. The break-in was performed at 0.5 V, adjusting the relative humidity (RH) at both electrodes.[34,35] AEMFC tests were carried out with three different cathodes: a) 40wt%Pt/C, with a loading of 0.45 mg_{Pt} cm^{-2} (total catalyst loading of 1.125 mg cm^{-2}); b) $Fe_{0.5}$-NH_3; and c) α-Mn_2O_3/$Fe_{0.5}$-NH_3 (20 wt % α-Mn_2O_3). Both b) and c) had a total catalyst loading of 1.5 mg cm^{-2}. All AEMFC experiments were carried out using 40wt%[PtRu]/C at the anode side (Pt:Ru 2:1 mass ratio) with a loading of 0.9 mg_{PGM} cm^{-2}.

Results and discussion

Physical and morphological characterization of Mn-oxides

The XRPD patterns shown in **Figure 1a** demonstrate the formation of pure or almost pure Mn-oxide phases. All diffraction peaks could be assigned to the targeted oxide phase (**Figure S1**), except for the α-Mn_2O_3 pattern which also shows minor peaks that can be assigned to α-MnO_2 (5% of α-MnO_2 was estimated,[85]). **Figure 1a** also underlines the higher crystallite dimension of α-Mn_2O_3 compared to MnO_2 structures. The δ-MnO_2 phase, especially, shows broad peaks indicating small crystallite. The high crystallinity of the present α-Mn_2O_3 material may be related to the high temperature of 550°C at which it was formed (see Experimental section), while the higher crystallinity of β-MnO_2 relative to δ-MnO_2 may also be explained from the viewpoint of the synthesis temperature, namely room temperature for δ-MnO_2 and then calcination at 450°C to obtain β-MnO_2. **Figure 1b** shows the N_2 adsorption isotherms of the Mn-oxide materials, revealing the coexistence of micro and mesopores. The isotherm of δ-MnO_2 shows the highest amount of N_2 adsorbed, especially at low P/P_0 and also a strong hysteresis closing at P/P_0 of *ca* 0.4. The shape of the isotherms of β-MnO_2 and α-MnO_2 are similar up to P/P_0 = 0.7, with the one for β-MnO_2 vertically translated by *ca* +10 $cm^3 \cdot g^{-1}$ due to a higher amount of N_2 adsorbed at low P/P_0. The adsorption isotherm for α-Mn_2O_3 clearly shows a much lower amount of N_2 adsorbed relative to all others, as well as little hysteresis, suggesting it is mostly non-porous. The BET specific surface areas are, in increasing order, 14 (α-Mn_2O_3), 98 (α-MnO_2), 136 (β-MnO_2) and 214 (δ-MnO_2) $m^2 \cdot g^{-1}$. In line with the very different BET areas, SEM micrographs provide evidence of substantial morphological differences. Macroscopically, δ-MnO_2 and β-MnO_2 share a common particle morphology, with a size in the range of 300-600 nm (**Figure 2a, c**), in line with the fact that β-MnO_2 was simply derived from δ-MnO_2 *via* calcination. However, the high resolution SEM micrographs show that the δ-MnO_2 surface has a higher roughness, with a sand-rose morphology and chambers of 30-60 nm, which partially collapsed in the case of the β-MnO_2 particles (**Figure 2**

b, d). The macroscopic morphology of α-MnO_2 is different, with large chunks that are several µm in size, composed of numerous well-defined rod-shaped sub-structures with ~130-300 nm length and 30-60 nm width, and also of even smaller objects with less-defined particle-like morphology (**Figure 2 e, f**). Last, α-Mn_2O_3 has an molten-like, interconnected particle morphology with a smooth surface and an average particle dimension of ~150 nm (**Figure 2 g, h**), in line with the higher temperature of 550°C used for its synthesis. The BET area ranking can be reasonably well explained from the surface roughness as identified by the higher magnification SEM images. The highest BET area was measured for δ-MnO_2 (214 $m^2 \cdot g^{-1}$) with highest surface roughness (**Figure 2b**), then slightly decreased BET area of 136 $m^2 \cdot g^{-1}$ for β-MnO_2 due to partial collapse of surface tortuosity (**Figure 2d**), still a high surface area of 98 $m^2 \cdot g^{-1}$ for α-MnO_2 with smooth but small rod substructures (**Figure 2f**) and, last, drastically lowered BET area of 14 $m^2 \cdot g^{-1}$ for α-Mn_2O_3 due to interconnected and molten particles morphology (**Figure 2h**).

To further verify the apparent correlation between surface roughness and BET area, we calculated the expected size of Mn-oxide nanostructures from their measured BET areas and assuming either a slab, rod, or spherical geometry (depending on samples) for the non-porous oxide substructures assumed to contribute mainly to the surface area of the Mn-oxides (**Table 1**). For δ-MnO_2 and β-MnO_2, the assumed slab geometry results in an estimated slab thickness of *ca* 3 nm, in line with the very thin walls of the sand rose morphology observed by SEM.

For α-MnO_2, the assumed rod morphology results in *ca* 9 nm diameter for the rods, which is significantly smaller than observed by SEM. Therefore, the surface of α-MnO_2 seems to result from a contribution of the observed rods but also from the smaller and less defined objects seen in the SEM images (**Figure 2f**). Last, for α-Mn_2O_3, the estimated particle size of *ca* 95 nm is in line with the smooth particles observed in SEM images (**Figure 2h**). Due to these large morphological differences, the apparent activity that will be measured for a given loading of Mn-Oxides during

RDE measurements needs to be normalized to the active area, which will be approximated by the BET area.

Electrochemical characterization of Mn-oxides

The HPRR activity of the four Mn-oxide polymorphs mixed either with Vulcan (**Figure 3a**) or $Fe_{0.5}$-NH_3 (**Figure 3b**) was investigated by RDE in deaerated 0.1 M KOH with 2 mM HO_2^-. The polarization curves seen in **Figure 3a-b** show a cathodic branch that can mainly be assigned to HPRR (Eq. 1), and an anodic branch that can be assigned to the hydrogen peroxide oxidation reaction (HPOR) (Eq. 2). In addition, a minor fraction of the cathodic current might also be related to the ORR, with O_2 being produced *in situ* via non-electrochemical disproportionation of peroxide on the Mn-oxide surface (Eq. 3).

$HO_2^- + H_2O + 2\ e^- \rightarrow 3\ OH^-$; $E^0 \sim 1.73$ V *vs.* RHE at pH 13 (1)

$HO_2^- + OH^- \rightarrow O_2 + H_2O + 2e^-$; $E^0 \sim 0.72$ V *vs.* RHE at pH 13 (2)

$2\ HO_2^- \rightarrow 2\ OH^- + O_2$ (3)

Considering the electrochemical reactions, it is important to note that reaction 2 is not the reverse of reaction 1, and the HPRR and HPOR have therefore very different equilibrium potentials, at pH 13 (see the equations above).[90] This expresses that, in the entire potential region between 0.72 and 1.73 V *vs.* RHE, HO_2^- should be highly unstable and could, theoretically, be at the same time electro-oxidized to O_2 and electro-reduced to OH^-. In practice, however, a net oxidation current is generally observed at potentials above 0.8-0.9 V, depending on the electrocatalyst investigated, and assigned to HPOR.[83,91] The oxidation reaction (2) may be kinetically much faster than the reduction reaction (1), explaining why a net positive current is observed on all types of catalysts in that potential region. A net reduction current is observed for MnO_x/Vulcan only when the HPOR becomes thermodynamically unfavored, *i.e.* at potentials lower than 0.83-0.85 V *vs.* RHE (**Figure**

3a). At those conditions, peroxide anions at the electrode surface can no longer be oxidized, and become available for HPRR. No clear redox process associated with Mn-oxides is observed near the open circuit potential of 0.83-0.85 V *vs.* RHE, except for δ-MnO_2, as shown by cyclic voltammetry in a N_2-saturated electrolyte free of peroxide (**Figure S2**). Therefore, the experimental values of open circuit potential (OCP) should be close to the equilibrium potential of reaction (2). With 2 mM HO_2^- in the electrolyte and assuming an activity of 1 for O_2 (*i.e.* assuming that reaction 3 can saturate with O_2 in a very thin layer of electrolyte near the catalyst surface), one can calculate from the Nernst equation that the equilibrium potential for reaction (2) should be 0.801 V *vs.* RHE, assuming a pH of 13. This is close to the experimentally observed values of OCP, ranging from 0.83 to 0.85 V *vs.* RHE for δ-MnO_2, β-MnO_2, α-MnO_2 and α-Mn_2O_3, in the order of increasing OCP values. Looking at the cathodic branch, assigned mainly to HPRR, the current density reaches different values of plateau depending on the Mn-oxide considered (**Figure 3a**), which is in contradiction with a same diffusion-limited current density expected for the two-electron HPRR. During the HPRR, the current density plateau is highest for α-Mn_2O_3, followed by β-MnO_2 and δ-MnO_2, and lowest for α-MnO_2. It was shown by Ryabova *et al* that this limiting current density can be assigned entirely to a rate-determining chemical step in the HPRR on Mn_3O_4 and MnOOH (with the limiting current density showing no variation with the rotation rate), while β-MnO_2 was in an intermediate situation in which the limiting current density slightly varied with rotation rate, but much less than expected from the Levich equation.[83] In contrast, the limiting current density of HPRR on α-Mn_2O_3 obeyed the Levich equation and increased proportionally with the square root of the electrode rotation rate. The authors concluded that for MnOOH and Mn_3O_4 (as well as β-MnO_2, partially) the rate of the HPRR at low potential is not controlled by the diffusion of HO_2^- species toward the electrode, but by a slow chemical step. The latter was proposed to be the chemical dissociation of the O-O bond of an adsorbed HO_2^- on a Mn^{III} site. Our experimental results are in line with this, showing that other MnO_2 allotropes behave similarly to β-MnO_2 (**Figure 3a**). In the

anodic branch (where the HPOR dominates), in contrast, no such effect was reported by Ryabova *et al*, and the HPOR was limited by peroxide diffusion at potentials above 1 V *vs*. RHE for both α-Mn_2O_3 and β-MnO_2.[83] A similar observation is made here for oxidation current densities at 1 V *vs*. RHE on the present set of Mn-oxides mixed with Vulcan, though the anodic branches at this potential have not yet reached their plateau. This may be due to the lower OH^- concentration used in our work compared to Ref.[83] , 0.1 and 1.0 M respectively. As one can see from reaction (2), the HPOR involves OH^- as a reactant, and this could therefore impact the HPOR reaction rate.

As discussed in the previous section, the different Mn-oxides possess very different BET areas, α-Mn_2O_3 in particular having a lower BET area than the other materials. To assess their intrinsic activity for HPRR/HPOR, we normalized the geometric current density by the surface area of the oxides in the active layer (from the known loading and the known BET area of each oxide). Since Vulcan has negligible activity for HPRR/HPOR (**Figure 3a,** black diamonds), this normalization should correctly represent the intrinsic specific surface activity of the Mn-oxides in a three-electrode environment where the liquid electrolyte should wet the entire surface of all of the catalysts. **Figure 3c** highlights the superior intrinsic activity of α-Mn_2O_3 compared to the three MnO_2 allotropes. In this graph, α-Mn_2O_3 not only reaches higher reduction currents at low potential (due to non-limitation by a slow chemical step) but also higher oxidation and reduction currents near OCP, *i.e.* faster intrinsic electrochemical kinetics. To quantify the latter, we fitted the polarization curves in the region close to OCP (-30/+50 mV) with a straight line and report the derivative dj/dE (units of mA cm_{oxide}^{-2} V^{-1}) in **Figure 3d**. The figure shows a seven-fold higher intrinsic activity for α-Mn_2O_3 compared to β- and α-MnO_2, and fourteen-fold higher intrinsic activity compared to δ-MnO_2. These results are in line with the five-fold higher kinetic rate constants k_2 and k_3 for Mn_2O_3 vs. β-MnO_2 reported in Ref.[83], and describing the kinetics of reaction (2). In conclusion, α-Mn_2O_3 is shown to be intrinsically more active toward HPRR and HPOR than the other Mn-oxides. Furthermore, our recent study showed that Mn_2O_3 is also more stable than the other Mn-oxides in the ORR region, even after normalization for the oxide area.[85] Therefore, both

from activity and stability viewpoints, α-Mn_2O_3 is clearly identified as the most promising Mn-oxide material for scavenging peroxide species produced during ORR. The full potential of α-Mn_2O_3 *vs.* other Mn-oxides is, however, challenged by its generally lower BET area, related to the high temperature calcination usually required to form this phase.[92-94]

In the next step, the Mn-oxides were mixed with $Fe_{0.5}$-NH_3, in the same weight ratio as was used for Vulcan, *i.e.* 20 wt% Mn-oxide on $Fe_{0.5}$-NH_3. A SEM image of $Fe_{0.5}$-NH_3 is shown in **Figure S3a**, showing an alveolar structure in that region of the catalyst. Due to the commensurate sizes of the $Fe_{0.5}$-NH_3 and MnO_x particles materials (**Figure 2**), distinguishing the two phases is difficult in SEM images of the composite catalysts. As an example, **Figures S3b-c** show SEM images of α-Mn_2O_3/$Fe_{0.5}$-NH_3, where some particles, due to their different morphology can likely be assigned to α-Mn_2O_3. **Table S1** reports the elemental contents determined by SEM-EDX on different regions of α-Mn_2O_3/$Fe_{0.5}$-NH_3, revealing areas with Mn and Fe weight contents close to those expected for a homogeneous distribution of Mn_2O_3 on $Fe_{0.5}$-NH_3, as well as areas with lower-than-expected Mn contents. The HPRR and HPOR polarization curves of $Fe_{0.5}$-NH_3 and of the four composite materials are shown in **Figure 3b**, confirming the previously discussed feature of cathode limiting current density but also revealing a new feature with respect to trends in the OCP values. The $Fe_{0.5}$-NH_3 catalyst alone, while showing a much higher OCP value (*ca* 0.94 V *vs.* RHE) compared to all MnO_x/Vulcan, has poor HPRR and HPOR kinetics, as visible from its lower dj/dE near OCP and lower absolute value of cathodic current density at low potential (**Figure 3a-b**). The poor HPRR and HPOR activity of $Fe_{0.5}$-NH_3 is a general phenomenon for FeNC catalysts, observed in both alkaline and acid electrolytes.[95-101] The maximum HPOR and HPRR current densities for $Fe_{0.5}$-NH_3 in the potential range 0.5 – 1.0 V *vs.* RHE are *ca* 0.2 and 0.4 mA cm^{-2}, respectively (**Figure 3b**). These values are significantly increased for the MnO_x/$Fe_{0.5}$-NH_3 composites. In the cathodic region, the limiting current density increases in the same order than for the MnO_x/Vulcan catalysts, *i.e.* α-MnO_2 < δ-MnO_2 = β-MnO_2 < α-Mn_2O_3, demonstrating the role of Mn-oxides in increasing the HPRR activity of MnO_x/$Fe_{0.5}$-NH_3 composites. In the anodic region of 0.95 – 1.0 V

vs. RHE, the HPOR current density is also higher for all $MnO_x/Fe_{0.5}$-NH_3 composites relative to $Fe_{0.5}$-NH_3 (**Figure 3b**). The composites $MnO_x/Fe_{0.5}$-NH_3 also show higher OCP values than the corresponding MnO_x/Vulcan layers, with OCP values of 0.86 and 0.91 V *vs*. RHE for α-$MnO_2/Fe_{0.5}$-NH_3 and α-$Mn_2O_3/Fe_{0.5}$-NH_3, respectively. This shift of OCP toward higher values seems driven by the even higher OCP of $Fe_{0.5}$-NH_3 (0.94 V *vs.* RHE). In fact, due to the negligible activity of Vulcan in MnO_x/Vulcan layers, and the comparable loading of $Fe_{0.5}$-NH_3 in the pure $Fe_{0.5}$-NH_3 layer and in the composite $MnO_x/Fe_{0.5}$-NH_3 layers (0.20 and 0.16 mg cm^{-2}, respectively), one may expect the polarization curves of $MnO_x/Fe_{0.5}$-NH_3 layers to behave, in first approximation, as the linear superposition of the polarization curves of MnO_x/Vulcan and $Fe_{0.5}$-NH_3.

Overall, the results confirm the higher HPRR activity of α-$Mn_2O_3/Fe_{0.5}$-NH_3 relative to $Fe_{0.5}$-NH_3 itself, at potentials of 0.50 - 0.85 V *vs.* RHE. At the cathode of an AEMFC, peroxide may be produced in this potential region due to high current density and relatively low selectivity of metal-free N-doped sites (along with some peroxide produced from FeN_x sites).

The demonstration of the concept of scavenging HO_2^- formed during ORR with the addition of Mn-oxides to $Fe_{0.5}$-NH_3 requires RRDE measurements in O_2-saturated electrolyte. **Figure 4a, b** and **c** shows, for reference, the ORR selectivity, activity, and Tafel plots of MnO_x/Vulcan layers, respectively. The ORR onset of MnO_x/Vulcan layers is *ca* 0.9 V *vs.* RHE for α-Mn_2O_3, α- and β-MnO_2 and *ca* 20 mV lower for δ-MnO_2. The ORR polarization curves show otherwise a similar shape and reach comparable O_2-diffusion-limited current densities (**Figure 4b**). The latter are close to the value expected for an overall apparent four-electron ORR, correlated by low % HO_2^- detected at the ring (**Figure 4a**). A closer detail at the % HO_2^- reveals fine differences, with decreasing % HO_2^- in the order α-MnO_2, δ-MnO_2, β-MnO_2, α-Mn_2O_3. This is in the exact same order as the absolute value of limiting current density observed on MnOx/C layers in the HPRR measurement (**Figure 3a**). This suggests that ORR on these MnO_x proceeds *via* a 2e + 2e pathway (subsequent 2 electron reduction on same MnO_x sites) and/or via 2 electron pathway to peroxide followed by

catalytic HO_2^- decomposition (reaction 3), which could also lead to apparent overall near four-electron ORR.

Then, the ORR selectivity, polarization curves and Tafel plots were recorded for $Fe_{0.5}$-NH_3 and the four $MnO_x/Fe_{0.5}$-NH_3 composite layers (**Figure 5a, b** and **c**). $Fe_{0.5}$-NH_3 alone shows high ORR activity of *ca* 1 mA·cm^{-2} at 0.9 V *vs.* RHE (**Figure 5c**), *i.e.* a mass activity of *ca* 5 A·g^{-1}, similar to our recent study on $Fe_{0.5}$-NH_3 in alkaline electrolyte.[43] The ORR activity (in mA per cm^2 geometric area of electrode) at 0.9 V of the four $MnO_x/Fe_{0.5}$-NH_3 composite layers is *ca* 30 % lower (**Figure 5c**), as expected from the slightly lower loading of $Fe_{0.5}$-NH_3 in the composite cathodes(only 0.16 mg_{FeNC} cm^{-2}, while the reference $Fe_{0.5}$-NH_3 layer has 0.2 mg_{FeNC} cm^{-2}). Last but not least, **Figure 5a** demonstrates higher selectivity for all $MnO_x/Fe_{0.5}$-NH_3 composite layers relative to $Fe_{0.5}$-NH_3. This result can be interpreted as a bifunctional effect of the composite layers, the FeN_x sites mainly driving the ORR to water, with minute amount of peroxide produced (either on some FeN_x sites, or on the N-C surface), and the MnO_x particles mainly acting as electrochemical scavengers of the minute amount of peroxide produced.

Then, the stability of the composite catalyst α-$Mn_2O_3/Fe_{0.5}$-NH_3 was evaluated in *operando* SFC-ICP/MS. α-Mn_2O_3 was selected for the composite catalyst due its higher oxide-surface-normalized HPRR activity, as shown in this study and previously, as well as its slightly higher stability among this set of four oxides, as recently reported by Speck *et al.*[85]

Figure 6a (middle panel) in the region from 0 to *ca* 500 s shows similarly low Mn dissolution rates (< *ca* 0.1 ng·cm^{-2}·s^{-1}) for the composite α-$Mn_2O_3/Fe_{0.5}$-NH_3 catalyst in both Ar- and O_2-saturated electrolytes when the potential is cycled for the first time between 1 and 0.6 V *vs.* RHE. This is due to the relative thermodynamic stability of α-Mn_2O_3 in that restricted potential range. In contrast, when the potential is cycled between 1 and 0 V (time between 500 and 1500 s in **Figure 6a,** middle panel), the Mn leaching rates increased when compared to the 1-0.6 V cycling and a higher Mn leaching rate is observed in O_2-saturated electrolyte vs. Ar-saturated electrolyte. This trend is similar to that observed for α-Mn_2O_3/C.[85] An accelerated stress test protocol showed

that the overall dissolution of manganese in O_2-saturated electrolyte is higher than in Ar-saturated electrolyte (**Figure 6b,** middle panel), which is explained by the presence of hydrogen peroxide produced in O_2-saturated solution, as already reported by us.[85] Concerning Fe dissolution, the catalyst does not show evident dissolution peaks during the first slow scan between 1 and 0 V in O_2-saturated electrolyte (**Figure 6b**, bottom panel). The dissolution rate of Fe is 0.05-0.08 ng $cm^{-2}\cdot s^{-1}$, comparable to the Fe leaching rate observed for $Fe_{0.5}$-NH_3 and previously reported by us.[43] **Figure 6b** (middle panel) shows that the Mn dissolution rate from α-Mn_2O_3/$Fe_{0.5}$-NH_3 is comparable to the dissolution rate previously reported for the same Mn-oxide supported on Vulcan,[85] with maximum leaching rates of 0.15-0.30 ng$\cdot cm^{-2}\cdot s^{-1}$ in O_2-saturated electrolyte during the slow-scan from 1 to 0 V *vs*. RHE.

Finally, $Fe_{0.5}$-NH_3 and α-Mn_2O_3/$Fe_{0.5}$-NH_3 were evaluated as cathode catalysts in operating AEMFCs and compared to Pt/C (**Figure 7a**). The initial activity at 0.9 V of the PGM-free cathodes is comparable with that of Pt/C. $Fe_{0.5}$-NH_3 shows a higher current density at 0.9 V (65 mA$\cdot cm^{-2}$) than the composite catalyst, which shows 52 mA$\cdot cm^{-2}$, almost identical to Pt/C (55 mA$\cdot cm^{-2}$) (**Figure 7b**). At lower cell voltages, the PGM-free cathodes do not perform as well as the Pt/C cathode, due to mass transport issues. The latter may be assigned to a more difficult path for oxygen to reach the active centers in such cathodes (possibly due to the microporous nature of the carbon in $Fe_{0.5}$-NH_3), but also to local O_2 starvation due to the much lower site density in $Fe_{0.5}$-NH_3 (*ca* 1.6 wt % Fe only)[43] compared to Pt/C (40 wt% Pt). Nevertheless, the absolute performance obtained with these PGM-free cathodes is promising: the $Fe_{0.5}$-NH_3 and α-Mn_2O_3/$Fe_{0.5}$-NH_3 cathodes are able to support a current density of 1.43 A$\cdot cm^{-2}$ and 1.25 A$\cdot cm^{-2}$ at 0.6 V, respectively. This corresponds to 59 and 52 % of the current density at 0.6 V obtained with 0.45 $mg_{Pt}\cdot cm^{-2}$ (2.41 A$\cdot cm^{-2}$). The peak power density is 1.04 W$\cdot cm^{-2}$ for $Fe_{0.5}$-NH_3 and 0.98 W$\cdot cm^{-2}$ for the α-Mn_2O_3/$Fe_{0.5}$-NH_3 composite, compared to 1.53 W$\cdot cm^{-2}$ for Pt/C (**Figure 7c**). The higher current density at low potential (below 0.4 V) obtained using the composite α-Mn_2O_3/$Fe_{0.5}$-NH_3 cathode relative to $Fe_{0.5}$-NH_3 can be attributed either to the effect of the Mn-oxide helping in reducing peroxide into water at those

potentials, or to the slightly lower loading of $Fe_{0.5}$-NH_3 in the composite cathode (80% the loading compared to that in the $Fe_{0.5}$-NH_3 layer), helping the mass-transport of oxygen.

Table S2 gives an overview of AEMFC performance previously reported in H_2 and O_2 conditions with PGM-free cathodes, indicating three key metrics corresponding to pure kinetic control (current density at 0.9 V), mixed kinetic and mass-transport control (current density at 0.6 V) and mainly mass-transport control (peak power density) of the cell performance. From **Table S2**, it can be seen that the current densities reached at 0.9 V with the present $Fe_{0.5}$-NH_3 and α-Mn_2O_3/$Fe_{0.5}$-NH_3 cathodes (52-65 mA·cm^{-2}) are significantly above those reported for PGM-free metal oxides (≤15 mA·cm^{-2})[102-106] and other FeNC catalysts with atomically-dispersed FeN_x sites (≤25 mA·cm^{-2}),[107-111] with the exception of the material labelled Fe-S-Phen/CNT in Ref. [112] and that resulted in a current density of *ca* 120 mA·cm^{-2}. The latter was however reached at a cell temperature of 80°C, significantly above 60°C used in the present study. The current density at 0.6 V is an important operating point of fuel cells, often resulting in a balanced compromise between energy efficiency (proportional to the ratio of operating to thermodynamic cell voltage) and power density. The current density obtained with $Fe_{0.5}$-NH_3 and α-Mn_2O_3/$Fe_{0.5}$-NH_3 cathodes (1430 and 1250 mA·cm^{-2}) are above those reported for other FeNC cathodes (190-977 mA·cm^{-2}),[107,108,110-112] with two exceptions. The first, is a FeCoPc/C material in Ref. [109], that achieved 1670 mA·cm^{-2} at 0.6 V, though this was obtained at a higher cell temperature (80°C *vs.* 60°C here) and with a thinner AEM (15 µm, *vs.* 50 µm here). Both factors are known to significantly improve the cell performance, due to lower Ohmic resistance but also improved water management. The second exception was by our team using a similar FeNC material to $Fe_{0.5}$-NH_3[113], where a current density of 1830 mA·cm^{-2} was achieved at 65°C and 0.6 V. However, the data reported there was taken with a much higher IEC, thinner AEM based on high density polyethylene.[114]

The current density obtained with $Fe_{0.5}$-NH_3 and α-Mn_2O_3/$Fe_{0.5}$-NH_3 cathodes at 0.6 V (1430 and 1250 mA·cm^{-2}) are also above those reported recently for CoO and Co_3O_4 (320 and 520 mA cm^{-2}),[105,106] and comparable to those reported for CoO_x or cobalt ferrite (1330 and 1560 mA

cm^{-2})[103] and $MnCo_2O_4$ spinel (970 mA cm^{-2} at 60°C)[104]. The CoO_x and cobalt ferrite were tested in the same cell housing and with the same FC test bench as in the present study, although at slightly higher cell temperatures of 65 and 70°C (**Table S2**). Thus, in spite of a much higher ORR activity at 0.9 V for the present cathodes based on $Fe_{0.5}$-NH_3 *vs.* those based on cobalt-rich oxides, similar current densities are hitherto observed at 0.6 V. This reveals that mass-transport must be further optimized in $Fe_{0.5}$-NH_3 cathodes, in order to improve the catalyst utilization at high current density. This could be achieved with improved water management (thinner membrane, optimized cell and O_2 gas temperature and RH) or improved layer structure (pore size distribution, ionomer content and distribution, optimized catalyst loading). Finally, the peak power densities achieved with PGM-free cathodes are also reported in **Table S2**. A graph of peak power density *vs.* current density at 0.6 V of the data shown in **Table S2** would reveal a straight proportional relationship, such that a separate discussion is not necessary for the peak power density. A similar linear relationship is also visible in Figure 7b of Ref. [108].

Overall, this overview of recent AEMFC data with PGM-free cathodes highlights the kinetic advantage of the present $Fe_{0.5}$-NH_3 and α-Mn_2O_3/$Fe_{0.5}$-NH_3 cathodes over other PGM-free cathodes, and its state-of-the-art power density. Compared to the 2022 milestone of initial AEMFC performance recently defined by the U.S. Department of Energy (≥ 1000 mA cm^{-2} at 0.65 V on H_2/O_2, T ≥80°C and total PGM loading ≤ 0.2 mg cm^{-2}, see Table II in Ref. 8), the cell performance achieved at 60°C and at 0.65 V in the present work (1110 mA cm^{-2}) already slightly exceeds this milestone with a PGM-free cathode, but with a higher PGM loading than targeted in the MEA (*i.e.* at the anode). Improved cathode and cell performance by operating to higher temperature and with optimized conditions should, in the near future, leverage the reduction of the PGM loading at the anode while maintaining the same overall cell performance. The investigation of the durability of FeNC layers during AEMFC operation and their optimization for operation with air (CO_2-free) feed are the next important steps for increased maturity of FeNC-based AEMFC cathodes.

Conclusions

This study demonstrates that the addition of Mn-oxides to FeNC helps in scavenging hydrogen peroxide formed during ORR. The lower yields of hydrogen peroxide observed with $MnO_x/Fe_{0.5}$-NH_3 layers compared to $Fe_{0.5}$-NH_3 alone derives from the high HPRR kinetics of the four Mn-oxides. α-Mn_2O_3 was shown to have higher HPRR activity than the other three Mn-oxide polymorphs, once normalized per oxide surface area. The present α-Mn_2O_3 material has however lower BET area than the other Mn-oxides, and further progress could thus be made by synthesizing α-Mn_2O_3 powders with higher BET area. α-Mn_2O_3 was selected for stability study in *operando* SFC-ICP/MS. The results show similar dissolution rates for Mn and Fe from the mixed layer 20 wt% α-Mn_2O_3/ 80 wt% $Fe_{0.5}$-NH_3 when compared to 20wt% α-Mn_2O_3/C and $Fe_{0.5}$-NH_3, respectively. Thus, no synergy effect is observed regarding the metal leaching rates. The results also show similar trends as for the separate materials with respect to the saturating gas, with higher Mn dissolution rates in O_2 vs. Ar-saturated electrolytes, due the production of hydrogen peroxide that triggers the Mn leaching. Finally the mixed layer α-$Mn_2O_3/Fe_{0.5}$-NH_3 was tested at the cathode of an AEMFC, showing comparable activity at 0.9 V to the $Fe_{0.5}$-NH_3 cathode. The activity at 0.9 V in AEMFC is comparable to that achieved with a Pt/C cathode and significantly higher than that reported hitherto for cathodes based on cobalt-rich oxides. At 0.6 V cell voltage, current densities close to 1000 $mA \cdot cm^{-2}$ were achieved with α-$Mn_2O_3/Fe_{0.5}$-NH_3 and $Fe_{0.5}$-NH_3 cathodes at 60°C in H_2/O_2 conditions. This is comparable to the best results recently reported with cathodes based on cobalt-rich oxides. Further optimization of the mass-transport is necessary to increase the catalyst utilization at high current density, in order to fully exploit the kinetic advantage of FeNC *vs.* other PGM-based and PGM-free cathodes.

Acknowledgments

This work was supported by the European Union's Horizon 2020 research and innovation programme under grant agreement CREATE [721065]. We are grateful to Prof. John R. Varcoe (Univ. Surrey, UK) for providing the ETFE ionomer and membrane.

Figures

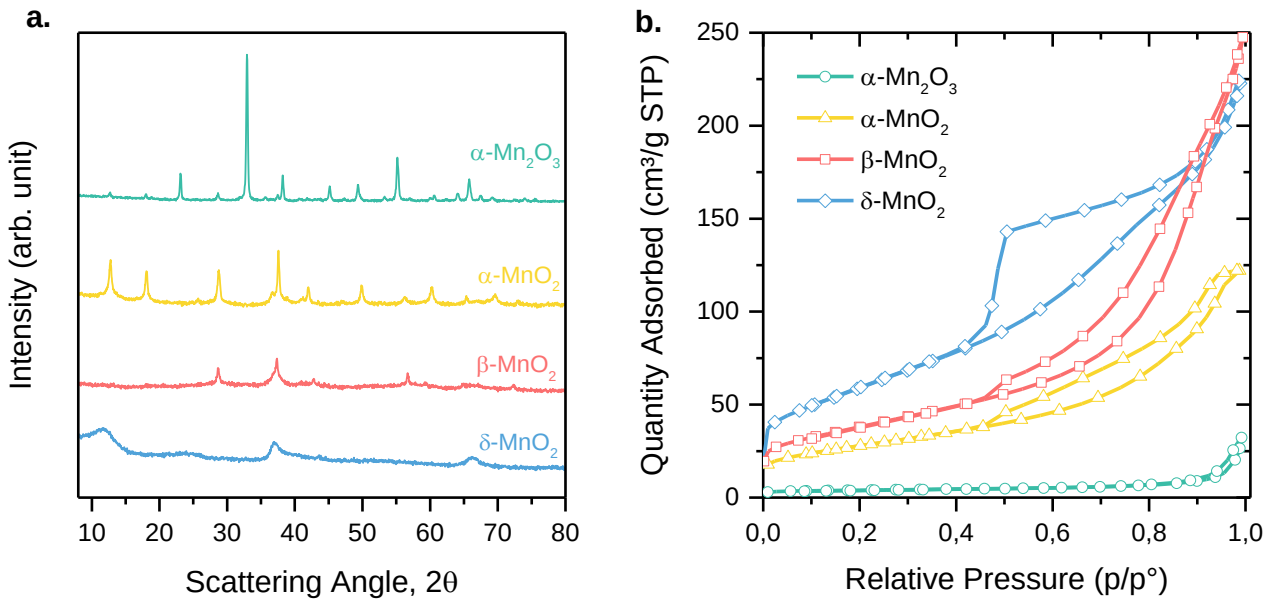

Figure 1. Physical characterization of the four Mn-oxides with (a) XRPD and (b) N_2 physisorption isotherms. The match with the calculated diffraction peaks for the targeted Mn-oxide structures can be seen in **Figure S1**.

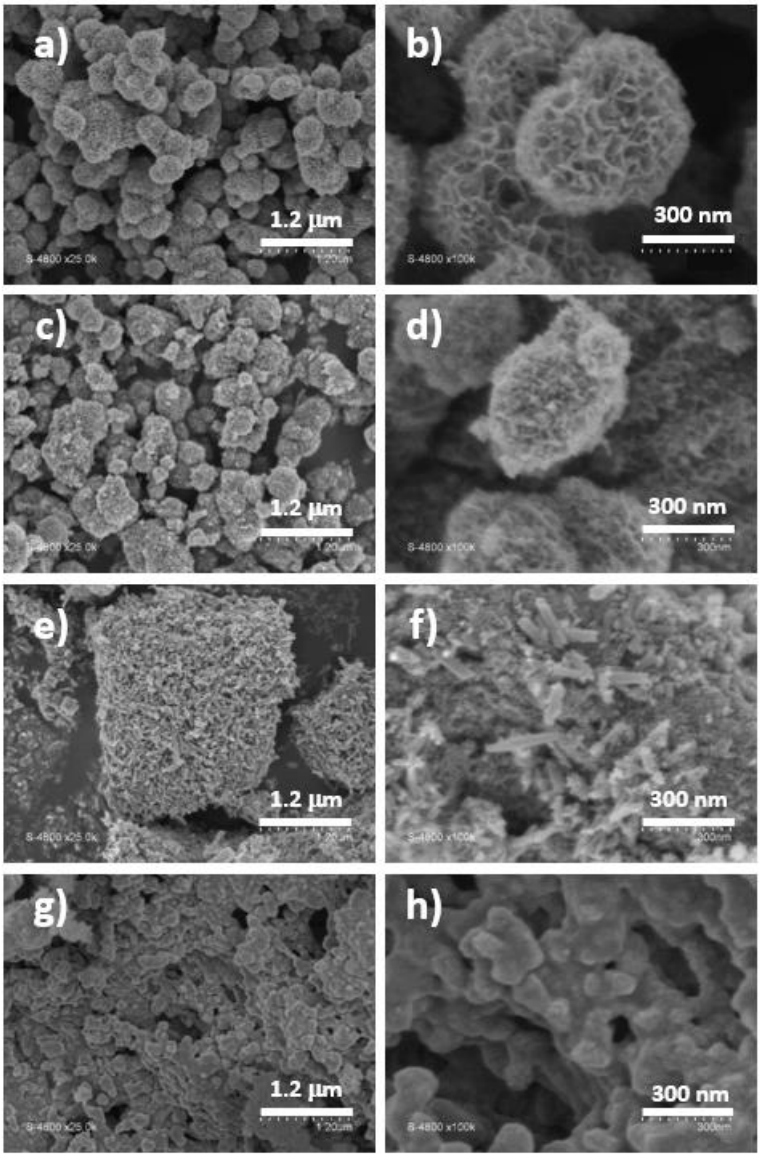

Figure 2. SEM micrographs of the different Mn-oxide polymorphs, in two different magnifications. a-b) δ-MnO_2, c-d) β-MnO_2 , e-f) α-MnO_2 , g-h) α-Mn_2O_3.

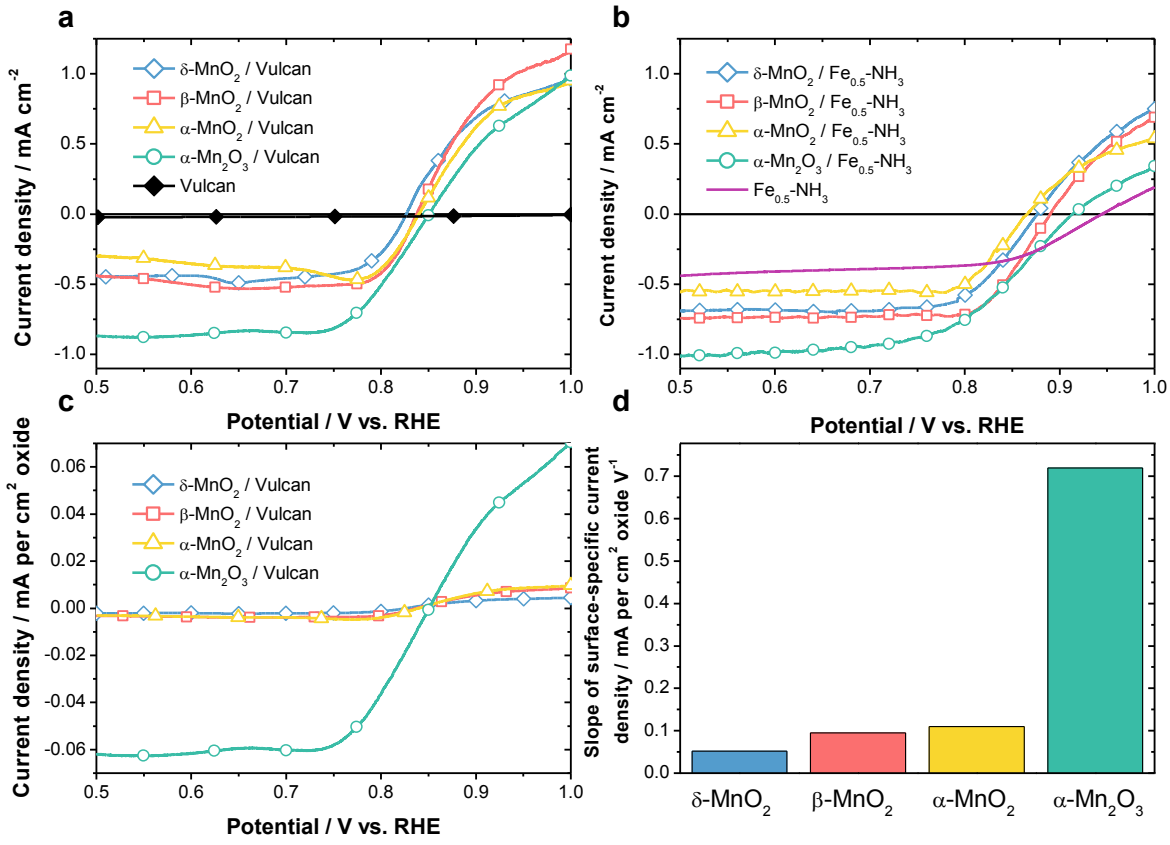

Figure 3. Activity toward HPRR. a) Polarization curves of the four Mn-oxides mixed with Vulcan (20 wt% MnO_x/C), b) polarization curves of the four Mn-oxides supported on $Fe_{0.5}$-NH_3 (20 wt% MnO_x/$Fe_{0.5}$-NH_3), c) polarisation curves of MnO_x/C normalized by the area of the Mn-oxides, d) histograms reporting the slope near j = 0 obtained from the BET-normalized polarization curves in c). All experiments were carried out in 2mM HO_2^- + 0.1 M KOH, with a three-electrode RDE configuration at a rotation rate of 1600 rpm, scan rate of 1 $mV \cdot s^{-1}$ and a total catalyst loading of 0.2 mg cm^{-2}.

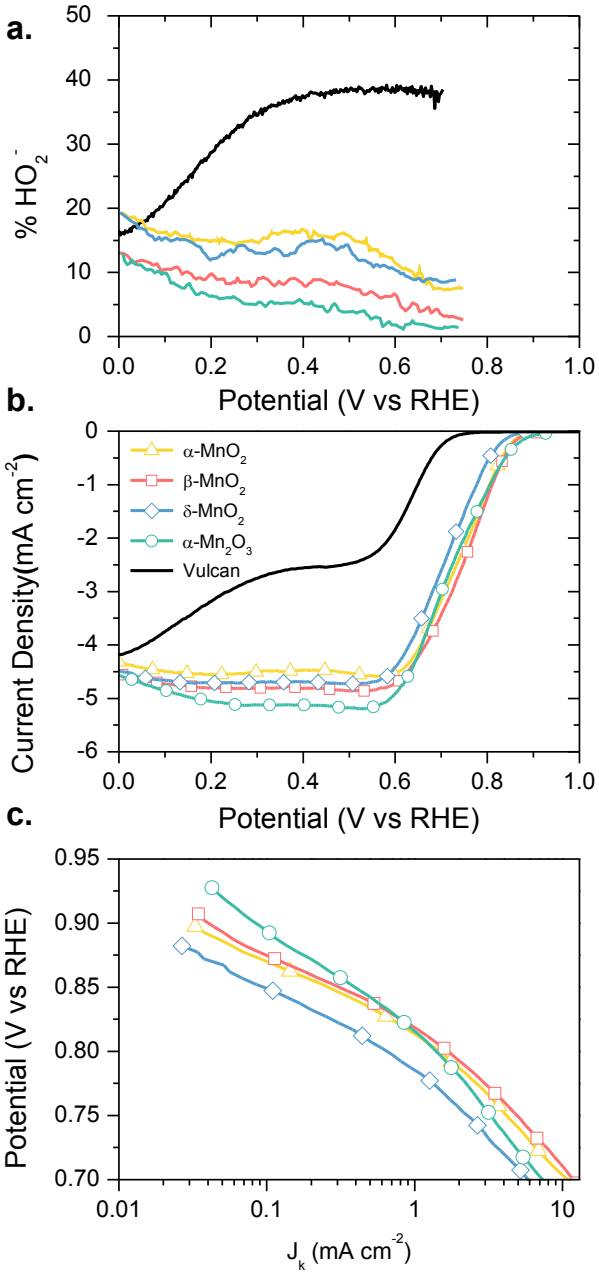

Figure 4. ORR selectivity, polarisation curves and Tafel plots for the four Mn-oxides supported on Vulcan carbon (20 wt% MnO_x / Vulcan). The total catalyst loading is 0.2 mg·cm^{-2}, except for Vulcan alone, with a carbon loading of 0.16 mg·cm^{-2} mimicking the amount of Vulcan deposited with the MnO_x/Vulcan active layers. All experiments were carried out in O_2 saturated 0.1 M KOH electrolyte, with a three-electrode RRDE configuration at a rotation rate of 1600 rpm and a scan rate of 1 mV·s^{-1}. No correction was made for the Ohmic drop.

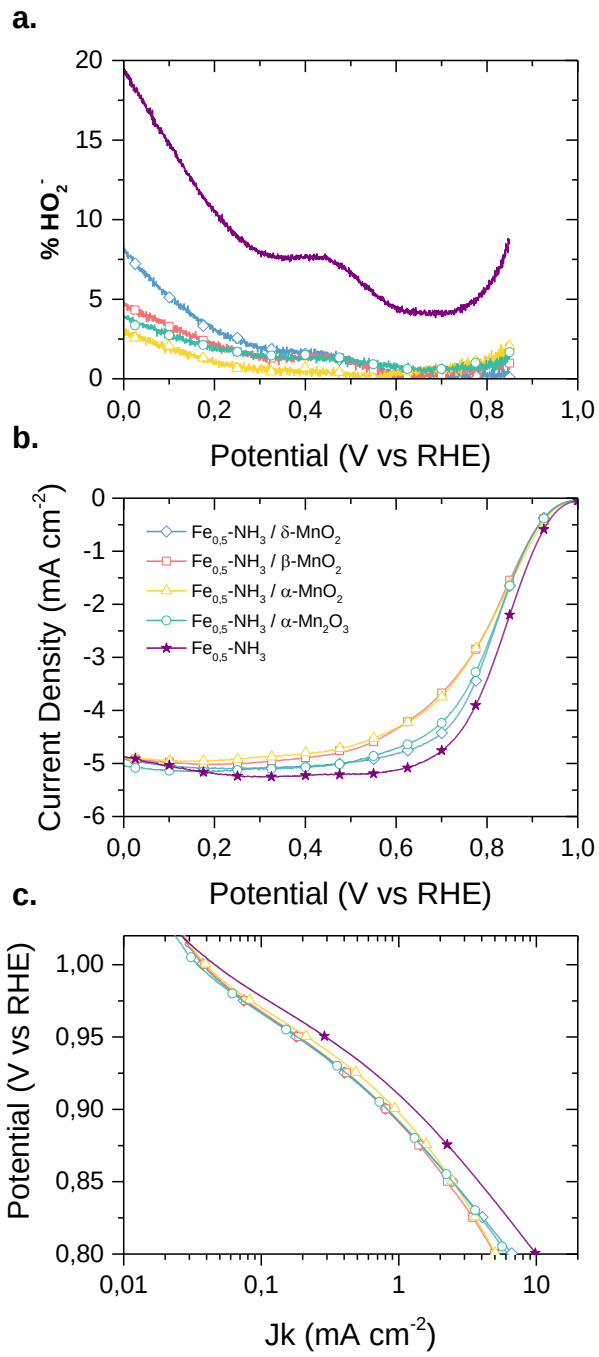

Figure 5. ORR selectivity, polarisation curves and Tafel plots for the four Mn-oxides supported on $Fe_{0.5}$-NH_3 (20 wt% MnO_x / $Fe_{0.5}$-NH_3). The total catalyst loading is 0.2 mg cm^{-2} (*i.e.* 0.2 mg_{FeNC} cm^{-2} for the pure layer, and only 0.16 mg_{FeNC} cm^{-2} for the composite layers). All experiments were carried out in O_2 saturated 0.1 M KOH electrolyte, with a three-electrode RRDE configuration at a rotation rate of 1600 rpm and a scan rate of 1 $mV \cdot s^{-1}$. No correction was made for Ohmic drop.

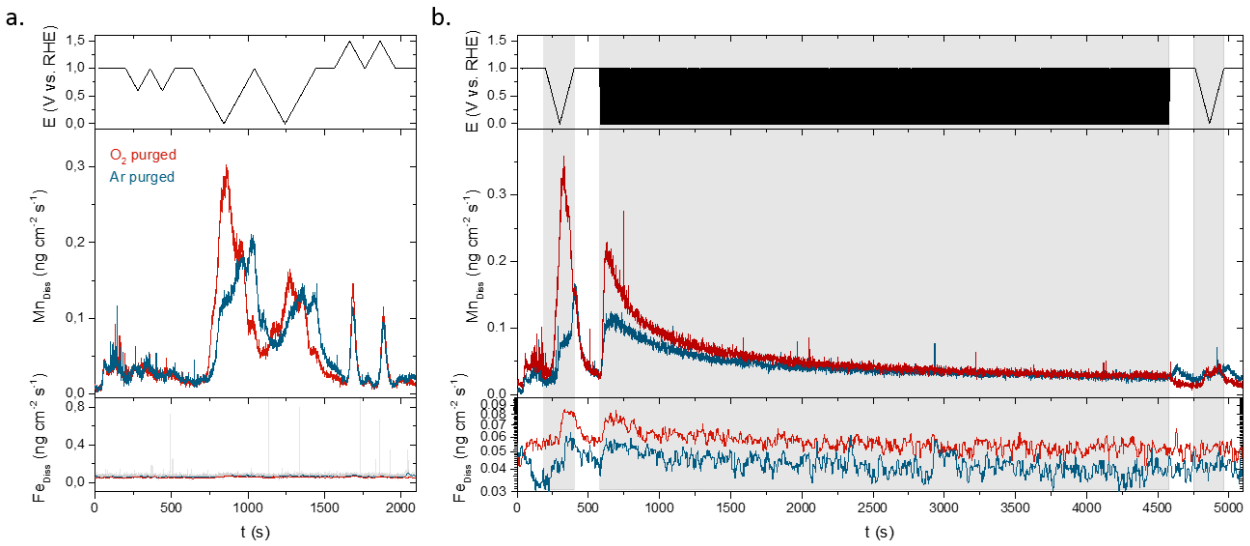

Figure 6 *Operando* SFC-ICP/MS of the composite catalyst 20% α-Mn_2O_3/80%$Fe_{0.5}$-NH_3 in alkaline electrolyte saturated with Ar (blue curve) or O_2 (red curve). a) Relation between the potential and the dissolution of manganese (middle graph) or iron (bottom graph) during low-load CVs (1-0.6 V *vs.* RHE) and high-load CVs (1-0 V *vs.* RHE) in either Ar- (blue curve) or O_2-saturated (red curve) electrolyte. b) Durability test comprising an initial high-load CV followed by fast CVs and a final high-load CV to evaluate the leaching of manganese (middle plot) and iron (bottom plot) in either Ar- (blue curve) or O_2-saturated (red curve) electrolyte.

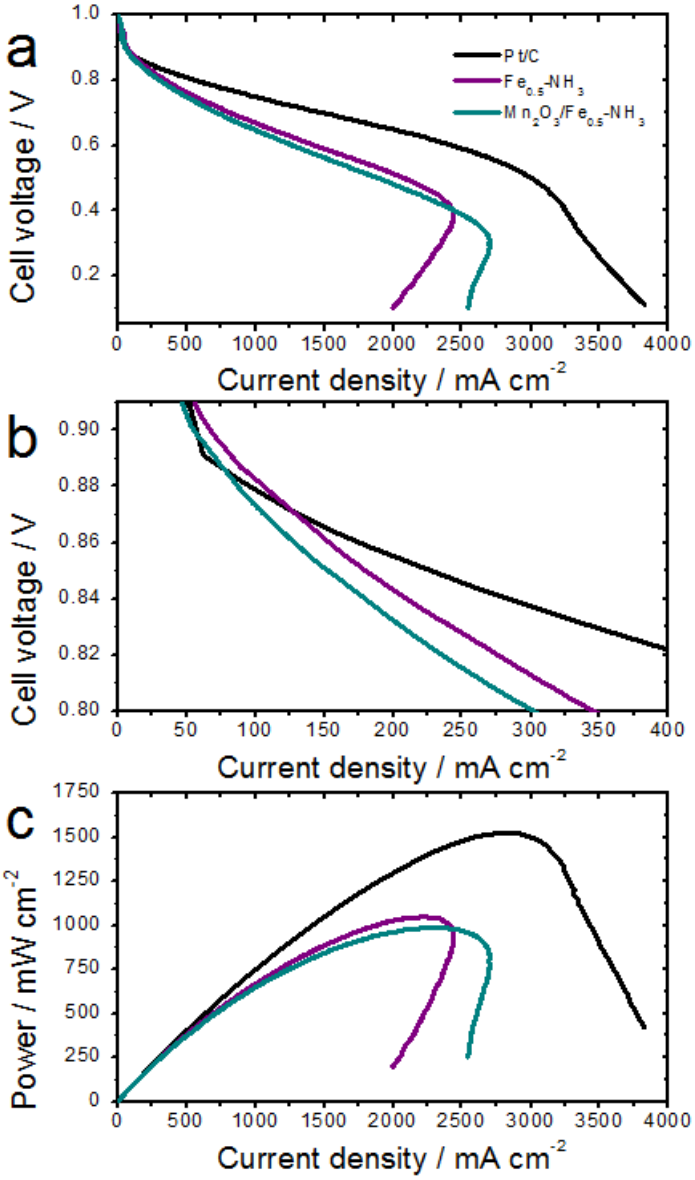

Figure 7. AEMFC polarization curves measured for Pt/C, $Fe_{0.5}$-NH_3 and α-Mn_2O_3/$Fe_{0.5}$-NH_3 cathodes using ETFE membrane and ETFE ionomer at a cell temperature of 60°C and using H_2 and O_2 flow rates of 1 L min^{-1}. The anode was always PtRu/C with 0.9 mg_{PtRu} cm^{-2}. The polarization curve was acquired at a scan rate of 10 $mV \cdot s^{-1}$ and the data recorded in the negative-going scan is shown. The cathode loading was 0.45 $mg_{Pt} \cdot cm^{-2}$ for Pt/C, 1.5 $mg_{FeNC} \cdot cm^{-2}$ for $Fe_{0.5}$-NH_3, and 0.3 mg $_{\alpha\text{-}Mn2O3} \cdot cm^{-2}$ and 1.2 $mg_{FeNC} \cdot cm^{-2}$ for α-Mn_2O_3/$Fe_{0.5}$-NH_3. No correction was made for Ohmic drop.

Tables

Oxide	BET ($m^2 \cdot g^{-1}$)	Density ($g \cdot cm^{-3}$)	Theor. specific surface area	Calculated object size / nm
δ-MnO_2	214	3.00	2 / (ρ·t) (slab)	3.1
β-MnO_2	136	5.03	2 / (ρ·t) (slab)	2.9
α-MnO_2	98	4.36	4 / (ρ·d) (rod)	9.4
α-Mn_2O_3	14	4.50	6 / (ρ·d) (sphere)	95.2

Table 1. Measured BET areas of the Mn-oxides and estimated object size of the oxide nanostructures forming the BET area. A slab geometry was assumed for δ-MnO_2 and β-MnO_2 and spherical geometry for α-Mn_2O_3.

References

1 Staffell, I., Scammam D., Velazquez Abad, A., Balcombe, P., Dodds, P. F., Ekins, P., Shah, N., Ward, K. R. The role of hydrogen and fuel cells in the global energy system. *Energy & Environmental Science* **12**, 463-491, (2019) doi:10.1039/C8EE01157E.

2 Stephens, I. E. L., Rossmeisl, J. & Chorkendorff, I. Toward sustainable fuel cells. *Science* **354**, 1378-1379 (2016).

3 Cano, Z. P., Banham, D., Ye, S., Hintennach, A., Lu, J., Fowler, M., Chen, Z. Batteries and fuel cells for emerging electric vehicle markets. *Nature Energy* **3**, 279-289, (2018) doi:10.1038/s41560-018-0108-1.

4 Kongkanand, A. & Mathias, M. F. The Priority and Challenge of High-Power Performance of Low-Platinum Proton-Exchange Membrane Fuel Cells. *The Journal of Physical Chemistry Letters* **7**, 1127-1137 (2016), doi:10.1021/acs.jpclett.6b00216.

5 Wu, J., Yuan, X. Z., Martin , J. J., Wang, H., Zhang, J., Shen, J., Wu, S., Merida, W. A review of PEM fuel cell durability: Degradation mechanisms and mitigation strategies. *Journal of Power Sources* **184**, 104-119, (2008) doi:10.1016/j.jpowsour.2008.06.006.

6 Gasteiger, H. A., Kocha, S. S., Sompalli, B. & Wagner, F. T. Activity benchmarks and requirements for Pt, Pt-alloy, and non-Pt oxygen reduction catalysts for PEMFCs. *Applied Catalysis B: Environmental* **56**, 9-35, (2005) doi:10.1016/j.apcatb.2004.06.021.

7 Majlan, E. H., Rohendi, D., Daud, W. R. W., Husaini, T. & Haque, M. A. Electrode for proton exchange membrane fuel cells: A review. *Renewable and Sustainable Energy Reviews* **89**, 117-134, (2018) doi:10.1016/j.rser.2018.03.007.

8 Thompson, S. T., James, B. D., Huya-Kouadio, J. M., Houchins, C., DeSantis, D. A., Ahluwalia, R., Wilson, A. R., Kleen, G., Papageorgopoulos, D. Direct hydrogen fuel cell electric vehicle cost analysis: System and high-volume manufacturing description, validation, and outlook. *Journal of Power Sources* **399**, 304-313, (2018) doi:https://doi.org/10.1016/j.jpowsour.2018.07.100.

9 Henning, S., Ishikawa, H., Kühn, L., Herranz, J., Müller, E., Eychmüller, A., Schmidt, T. J. Unsupported Pt-Ni Aerogels with Enhanced High Current Performance and Durability in Fuel Cell Cathodes. *Angewandte Chemie* **129**, 10847-10850, (2017) doi:10.1002/ange.201704253.

10 Chung, D. Y., Yoo, J. M. & Sung, Y.-E. Highly Durable and Active Pt-Based Nanoscale Design for Fuel-Cell Oxygen-Reduction Electrocatalysts. *Advanced materials* **30**, 1704123, (2018) doi:10.1002/adma.201704123.

11 Ding, J., Ji, S., Wang, H., Key, J., Brett, D. J. L., Wang, R. Nano-engineered intrapores in nanoparticles of PtNi networks for increased oxygen reduction reaction activity. *Journal of Power Sources* **374**, 48-54, (2018) doi:https://doi.org/10.1016/j.jpowsour.2017.11.002.

12 Asset, T., Chattot, R., Fontana, M., Mercier-Guyon, B., Job, N., Dubau, L., Maillard, F. A Review on Recent Developments and Prospects for the Oxygen Reduction Reaction on Hollow Pt-alloy Nanoparticles. *ChemPhysChem* **19**, 1552-1567, (2018) doi:10.1002/cphc.201800153.

13 Ishikawa, H., Henning, S., Herranz, J., Eychmüller, A., Uchida, M., Schmidt, T. J. Tomographic analysis and modeling of polymer electrolyte fuel cell unsupported catalyst layers. *Journal of The Electrochemical Society* **165**, F7-F16 (2018).

14 Chattot, R., Le Bacq, O., Beermann, V., Kühl, S., Herranz, J., Henning, S., Kühn, L., Asset, T., Guétaz, L., Renou, G., Drnec, J., Bordet, P., Pasturel, A., Eychmüller, A., Schmidt, T. J., Strasser, P., Dubau, L., Maillard, F. Surface distortion as a unifying concept and descriptor in oxygen reduction reaction electrocatalysis. *Nature materials* **17**, 827 (2018).

15 Banham, D. & Ye, S. Current Status and Future Development of Catalyst Materials and Catalyst Layers for Proton Exchange Membrane Fuel Cells: An Industrial Perspective. *ACS Energy Letters* **2**, 629-638, (2017) doi:10.1021/acsenergylett.6b00644.

16 Lefèvre, M., Proietti, E., Jaouen, F. & Dodelet, J.-P. Iron-Based Catalysts with Improved Oxygen Reduction Activity in Polymer Electrolyte Fuel Cells. *Science* **324**, 71-74, (2009) doi:10.1126/science.1170051.

17 Li, J. & Jaouen, F. Structure and activity of metal-centered coordination sites in pyrolyzed metal–nitrogen–carbon catalysts for the electrochemical reduction of O2. *Current Opinion in Electrochemistry* **9**, 198-206, (2018) doi:10.1016/j.coelec.2018.03.039.

18 Shao, M., Chang, Q., Dodelet, J.-P. & Chenitz, R. Recent Advances in Electrocatalysts for Oxygen Reduction Reaction. *Chemical Reviews* **116**, 3594-3657, (2016) doi:10.1021/acs.chemrev.5b00462.

19 Shao, Y., Dodelet, J.-P., Wu, G. & Zelenay, P. PGM-Free Cathode Catalysts for PEM Fuel Cells: A Mini-Review on Stability Challenges. *Advanced materials* **31**, 1807615, (2019) doi:10.1002/adma.201807615.

20 Wang, X. X., Swihart, M. T. & Wu, G. Achievements, challenges and perspectives on cathode catalysts in proton exchange membrane fuel cells for transportation. *Nature Catalysis* **2**, 578 (2019).

21 Martinez, U., Komini Babu, S., Holby, E. F., Chung, H. T., Yin, X., Zelenay, P. Progress in the Development of Fe-Based PGM-Free Electrocatalysts for the Oxygen Reduction Reaction. *Advanced materials* **31**, 1806545, (2019) doi:10.1002/adma.201806545.

22 Chisaka, M., Ishihara, A., Ota, K.-i. & Muramoto, H. Synthesis of carbon-supported titanium oxynitride nanoparticles as cathode catalyst for polymer electrolyte fuel cells. *Electrochimica Acta* **113**, 735-740 (2013).

23 Chisaka, M., Ando, Y. & Muramoto, H. Facile Combustion Synthesis of Carbon-Supported Titanium Oxynitride to Catalyse Oxygen Reduction Reaction in Acidic Media. *Electrochimica Acta* **183**, 100-106, (2015) doi:https://doi.org/10.1016/j.electacta.2015.03.211.

24 Ishihara, A., Nagai, T., Ukita, K., Arao, M., Matsumoto, M., Yu, L., Nakamura, T., Sekizawa, O., Takagi, Y., Matsuzawa, K., Napporn, T. W., Mitsushima, S., Uruga, T., Yokoyama, T., Iwasawa, Y., Imai, H., Ota, K-I. Emergence of Oxygen Reduction Activity in Zirconium Oxide-Based Compounds in Acidic Media: Creation of Active Sites for the Oxygen Reduction Reaction. *The Journal of Physical Chemistry C* **123**, 18150-18159, (2019) doi:10.1021/acs.jpcc.9b02393.

25 Zhang, H., Chung, H. T., Cullen, D. A., Wagner, S., Kramm, U. I., More, K. L., Zelenay, P. High-performance fuel cell cathodes exclusively containing atomically dispersed iron active sites. *Energy & Environmental Science* **12**, 2548-2558, (2019) doi:10.1039/C9EE00877B.

26 Wagner, S., Auerbach, H., Tait, C. E., Martinaiou, I., Kumar, S. C. N., Kübel, C., Sergeev, I., Wille, H-C., Behrends, J., Wolny, J. A., Schünemann, V., Kramm, U. I. Elucidating the Structural Composition of an Fe–N–C Catalyst by Nuclear- and Electron-Resonance Techniques. *Angewandte Chemie* **131**, 10596-10602, (2019) doi:10.1002/ange.201903753.

27 Mineva, T., Matanovic, I., Atanassov, P., Sougrati, M-T., Stievano, L., Clémencey, M., Kochem, A., Latour, J-M., Jaouen, F. Understanding Active Sites in Pyrolyzed Fe–N–C Catalysts for Fuel Cell Cathodes by Bridging Density Functional Theory Calculations and 57Fe Mössbauer Spectroscopy. *ACS Catalysis*, 9359-9371, (2019) doi:10.1021/acscatal.9b02586.

28 Kneebone, J. L., Daifuku, S. L., Kehl, J. A., Wu, G., Chung, H. T., Hu, M. Y., Ercan Alp, E., More, K. L., Zelenay, P. A Combined Probe-Molecule, Mössbauer, Nuclear Resonance Vibrational Spectroscopy, and Density Functional Theory Approach for Evaluation of

Potential Iron Active Sites in an Oxygen Reduction Reaction Catalyst. *The Journal of Physical Chemistry C* **121**, 16283-16290, (2017) doi:10.1021/acs.jpcc.7b03779.

29 Kramm, U. I., Herrmann-Geppert, I., Behrends, J., Lips, K., Fiechter, S., Bogdanoff, P. On an Easy Way To Prepare Metal–Nitrogen Doped Carbon with Exclusive Presence of MeN4-type Sites Active for the ORR. *Journal of the American Chemical Society* **138**, 635-640, (2016) doi:10.1021/jacs.5b11015.

30 Jiang, R., Li, L., Sheng, T., Hu, G., Chen, Y., Wang, L., Edge-Site Engineering of Atomically Dispersed Fe–N4 by Selective C–N Bond Cleavage for Enhanced Oxygen Reduction Reaction Activities. *Journal of the American Chemical Society* **140**, 11594-11598, (2018) doi:10.1021/jacs.8b07294.

31 Jia, Q., Ramaswamy, N., Tylus, U., Strickland, K., Li, J., Serov, A., Artyushkova, K., Atanassov, P., Anibal, J., Gumeci, C., Calabrese Barton, S., Sougrati, M-T., Jaouen, F., Halevi, B., Mukerjee, S. Spectroscopic insights into the nature of active sites in iron–nitrogen–carbon electrocatalysts for oxygen reduction in acid. *Nano Energy* **29**, 65-82, (2016) doi:https://doi.org/10.1016/j.nanoen.2016.03.025.

32 Lai, Q., Zheng, L., Liang, Y., He, J., Zhao, J., Chen, J. Metal–Organic-Framework-Derived Fe-N/C Electrocatalyst with Five-Coordinated Fe-Nx Sites for Advanced Oxygen Reduction in Acid Media. *ACS Catalysis* **7**, 1655-1663, (2017) doi:10.1021/acscatal.6b02966.

33 Zhang, H., Hwang, S., Wang, M., Feng, Z., Karakalos, S., Luo, L., Qiao, Z., Xie, X., Wang, C., Su, D., Shao, Y., Wu, G. Single Atomic Iron Catalysts for Oxygen Reduction in Acidic Media: Particle Size Control and Thermal Activation. *Journal of the American Chemical Society* **139**, 14143-14149, (2017) doi:10.1021/jacs.7b06514.

34 Kumar, K., Gairola, P., Lions, M., Ranjbar-Sahraie, N., Mermoux, M., Dubau, L., Zitolo, A., Jaouen, F., Maillard, F. Physical and Chemical Considerations for Improving Catalytic Activity and Stability of Non-Precious-Metal Oxygen Reduction Reaction Catalysts. *ACS Catalysis* **8**, 11264-11276, (2018) doi:10.1021/acscatal.8b02934.

35 Zitolo, A., Goellner, V., Armel, V., Sougrati, M-T., Mineva, T., Stievano, L., Fonda, E., Jaouen, F. Identification of catalytic sites for oxygen reduction in iron- and nitrogen-doped graphene materials. *Nature materials* **14**, 937-942, (2015) doi:10.1038/nmat4367.

36 Zitolo, A., Ranjbar-Sahraie, N., Mineva, T., Li, J., Jia, Q., Stamatin, S., Harrington, G. F., Lyth, S. M., Krtil, P., Mukerjee, S., Fonda, E., Jaouen, F. Identification of catalytic sites in cobalt-nitrogen-carbon materials for the oxygen reduction reaction. *Nature communications* **8**, 957, (2017) doi:10.1038/s41467-017-01100-7.

37 Kattel, S., Atanassov, P. & Kiefer, B. Stability, Electronic and Magnetic Properties of In-Plane Defects in Graphene: A First-Principles Study. *The Journal of Physical Chemistry C* **116**, 8161-8166, (2012) doi:10.1021/jp2121609.

38 Yang, L., Cheng, D., Xu, H., Zeng, X., Wan, X., Shui, J., Xiang, Z., Cao, D. Unveiling the high-activity origin of single-atom iron catalysts for oxygen reduction reaction. *Proceedings of the National Academy of Sciences* **115**, 6626-6631, (2018). doi:10.1073/pnas.1800771115.

39 Holby, E. F., Wu, G., Zelenay, P. & Taylor, C. D. Structure of Fe–Nx–C Defects in Oxygen Reduction Reaction Catalysts from First-Principles Modeling. *The Journal of Physical Chemistry C* **118**, 14388-14393, (2014) doi:10.1021/jp503266h.

40 Banham, D., Ye, S., Pei, K., Ozaki, J-I., Kishimoto, T., Imashiro, Y. A review of the stability and durability of non-precious metal catalysts for the oxygen reduction reaction in proton exchange membrane fuel cells. *Journal of Power Sources* **285**, 334-348, (2015) doi:10.1016/j.jpowsour.2015.03.047.

41 Choi, C. H., Baldizzone, C., Polymeros, G., Pizzutilo, E., Kasian, O., Schuppert, A. K., Ranjbar Sahraie, N., Sograti, M-T., Mayrhofer, K. J. J., Jaouen, F. Minimizing Operando

Demetallation of Fe-N-C Electrocatalysts in Acidic Medium. *ACS Catalysis* **6**, 3136-3146, (2016) doi:10.1021/acscatal.6b00643.

42 Choi, C. H., Baldizzone, C., Grote, J-P., Schuppert, A. K., Jaouen, F., Mayrhofer, K. J. J. Stability of Fe-N-C Catalysts in Acidic Medium Studied by Operando Spectroscopy. *Angewandte Chemie* **54**, 12753-12757, (2015) doi:10.1002/anie.201504903.

43 Santori, P. G., Speck, F. D., Li, J., Zitolo, A., Jia, Q., Mukerjee, S., Cherevko, S. , Jaouen, F. Effect of Pyrolysis Atmosphere and Electrolyte pH on the Oxygen Reduction Activity, Stability and Spectroscopic Signature of FeNx Moieties in Fe-N-C Catalysts. *Journal of The Electrochemical Society* **166**, F3311-F3320, (2019) doi:10.1149/2.0371907jes.

44 Goellner, V., Armel, V., Zitolo, A., Fonda, E. & Jaouen, F. Degradation by Hydrogen Peroxide of Metal-Nitrogen-Carbon Catalysts for Oxygen Reduction. *Journal of The Electrochemical Society* **162**, H403-H414, (2015) doi:10.1149/2.1091506jes.

45 Choi, C. H., Lim, H-K., Chnug, M., Chon, G., Ranjbar Sahraie, N., Altin, A., Sougrati, M-T., Stievano, L., Oh, H. S., Park, E. S., Luo, F., Strasser, P. Drazic, G., Mayrhofer, K. J. J., Kim, H. Jaouen, F. The Achilles' heel of iron-based catalysts during oxygen reduction in an acidic medium. *Energy & Environmental Science* **11**, 3176-3182, (2018) doi:10.1039/c8ee01855c.

46 Wang, X. X., Prabhakaran, V., He, Y., Shao, Y. & Wu, G. Iron-Free Cathode Catalysts for Proton-Exchange-Membrane Fuel Cells: Cobalt Catalysts and the Peroxide Mitigation Approach. *Advanced materials* **31**, 1805126, (2019) doi:10.1002/adma.201805126.

47 Ferrandon, M., Wang, X., Kropf, J. A., Myers, D. J., Wu, G., Johnston, C. M., Zelenay, P. Stability of iron species in heat-treated polyaniline–iron–carbon polymer electrolyte fuel cell cathode catalysts. *Electrochimica Acta* **110**, 282-291, (2013) doi:https://doi.org/10.1016/j.electacta.2013.03.183.

48 Singh, H., Zhuang, S., Ingis, B., Nunna, B. B. & Lee, E. S. Carbon-based catalysts for oxygen reduction reaction: A review on degradation mechanisms. *Carbon* **151**, 160-174, (2019) doi:https://doi.org/10.1016/j.carbon.2019.05.075.

49 Martinez, U., Komini Babu, S., Holby, E. F. & Zelenay, P. Durability challenges and perspective in the development of PGM-free electrocatalysts for the oxygen reduction reaction. *Current Opinion in Electrochemistry* **9**, 224-232, (2018) doi:https://doi.org/10.1016/j.coelec.2018.04.010.

50 Serov, A., Artyushkova, K., Niangar, E., Wang, C., Dale, N., Jaouen, F., Sougrati, M-T., Jia, Q., Mukerjee, S., Atanassov, P. Nano-structured non-platinum catalysts for automotive fuel cell application. *Nano Energy* **16**, 293-300 (2015).

51 Kumar, K., Dubau, L., Mermoux, M., Li, J., Zitolo, A., Nelayah, J., Jaouen, F., Maillard, F. On the Influence of Oxygen on the Degradation of Fe-N-C Catalysts. *Angewandte Chemie International Edition* **59**, 3235-3243, (2020) doi:10.1002/anie.201912451.

52 Goellner, V., Baldizzone, C., Schuppert, A., Sougrati, M. T., Mayrhofer, K., Jaouen, F. Degradation of Fe/N/C catalysts upon high polarization in acid medium. *Physical chemistry chemical physics* **16**, 18454-18462, (2014) doi:10.1039/c4cp02882a.

53 Proietti, E., Jaouen, F., Lefèvre, M., Larouche, N., Tian, J., Herranz, J., Dodelet, J-P. Iron-based cathode catalyst with enhanced power density in polymer electrolyte membrane fuel cells. *Nature communications* **2**, 416, (2011) doi:10.1038/ncomms1427.

54 Yang, L., Larouche, N., Chenitz, R., Zhang, G., Lefèvre, M., Dodelet, J-P. Activity, Performance, and Durability for the Reduction of Oxygen in PEM Fuel Cells, of Fe/N/C Electrocatalysts Obtained from the Pyrolysis of Metal-Organic-Framework and Iron Porphyrin Precursors. *Electrochimica Acta* **159**, 184-197, (2015) doi:https://doi.org/10.1016/j.electacta.2015.01.201.

55 Chenitz, R., Kramm, U. I., Lefèvre, M., Glibin, V., Zhang, G., Sun, S., Dodelet, J-P. A specific demetalation of Fe–N4 catalytic sites in the micropores of NC_Ar + NH3 is at the origin of the initial activity loss of the highly active Fe/N/C catalyst used for the reduction of oxygen in PEM fuel cells. *Energy & Environmental Science* **11**, 365-382, (2018) doi:10.1039/c7ee02302b.

56 Herranz, J., Jaouen, F., Lefèvre, M., Kramm, U. I., Proietti, E., Dodelet, J-P., Bogdanoff, P., Fiechter, S., Abs-Wurmbach, I., Bertrand, P., Arruda, T. M., Mukerjee, S. Unveiling N-protonation and anion-binding effects on Fe/N/C-catalysts for O2 reduction in PEM fuel cells. *The journal of physical chemistry. C, Nanomaterials and interfaces* **115**, doi:10.1021/jp2042526 (2011).

57 Meng, H., Jaouen, F., Proietti, E., Lefèvre, M. & Dodelet, J.-P. pH-effect on oxygen reduction activity of Fe-based electro-catalysts. *Electrochemistry Communications* **11**, 1986-1989, (2009) doi:10.1016/j.elecom.2009.08.035.

58 Yasuda, S., Furuya, A., Uchibori, Y., Kim, J. & Murakoshi, K. Iron–Nitrogen-Doped Vertically Aligned Carbon Nanotube Electrocatalyst for the Oxygen Reduction Reaction. *Advanced Functional Materials* **26**, 738-744, (2016) doi:10.1002/adfm.201503613.

59 Sarapuu, A., Kreek, K., Kisand, K., Kook, M., Uibu, M., Koel, M., Tammeveski, K. Electrocatalysis of oxygen reduction by iron-containing nitrogen-doped carbon aerogels in alkaline solution. *Electrochimica Acta* **230**, 81-88, (2017) doi:https://doi.org/10.1016/j.electacta.2017.01.157.

60 Ratso, S., Kruusenberg, I., Sarapuu, A., Rauwel, P., Saar, R., Joost, U., Aruväli, J., Kanninen, P., Kallio, T., Tameveski, K. Enhanced oxygen reduction reaction activity of iron-containing nitrogen-doped carbon nanotubes for alkaline direct methanol fuel cell application. *Journal of Power Sources* **332**, 129-138, (2016) doi:https://doi.org/10.1016/j.jpowsour.2016.09.069.

61 Varcoe, J. R., Atanassov, P., Dekel, D. R., Herring, A. M., Hickner, M. A., Kohl, P. A., Kucernak, A. R., Mustain, W. E., Nijmeijer, K., Scoth, K., Xu, T., Zhuang, L. Anion-exchange membranes in electrochemical energy systems. *Energy & Environmental Science* **7**, 3135-3191, (2014) doi:10.1039/C4EE01303D.

62 Thompson, S. T., Peterson, D., Ho, D. & Papageorgopoulos, D. Perspective—The Next Decade of AEMFCs: Near-Term Targets to Accelerate Applied R&D. *Journal of The Electrochemical Society* **167**, 084514, (2020) doi:10.1149/1945-7111/ab8c88.

63 Setzler, B. P., Zhuang, Z., Wittkopf, J. A. & Yan, Y. Activity targets for nanostructured platinum-group-metal-free catalysts in hydroxide exchange membrane fuel cells. *Nature Nanotechnology* **11**, 1020-1025 (2016), doi:10.1038/nnano.2016.265.

64 Dekel, D. R. Review of cell performance in anion exchange membrane fuel cells. *Journal of Power Sources* **375**, 158-169, (2018) doi:10.1016/j.jpowsour.2017.07.117.

65 Gottesfeld, S., Dekel, D. R., Page, M., Bae, C., Yan, Y., Zelenay, P., Kim, Y. S. Anion exchange membrane fuel cells: Current status and remaining challenges. *Journal of Power Sources* **375**, 170-184, (2018) doi:10.1016/j.jpowsour.2017.08.010.

66 Wang, Y., Wang, G., Li, G., Huang, B., Pan, J., Liu, Q., Han, J., Xiao, L., Lu, J., Zhuang, L. Pt–Ru catalyzed hydrogen oxidation in alkaline media: oxophilic effect or electronic effect? *Energy & Environmental Science* **8**, 177-181, (2015) doi:10.1039/c4ee02564d.

67 Omasta, T. J., Park, A. M., LaManna, J. M., Zhang, Y., Peng, X., Wang, L., Jacobson, D. L., Varcoe, J. R., Hussey, D. S., Pivovar, B. S., Mustain, W. E. Beyond catalysis and membranes: visualizing and solving the challenge of electrode water accumulation and flooding in AEMFCs. *Energy & Environmental Science* **11**, 551-558,(2018) doi:10.1039/C8EE00122G.

68 Huang, G., Mandal, M., Peng, X., Yang-Neyerlin, A. C., Pivovar, B. S., Mustain, W. E., Kohl, P. A. Composite Poly(norbornene) Anion Conducting Membranes for Achieving Durability, Water Management and High Power (3.4 W/cm2) in Hydrogen/Oxygen Alkaline Fuel Cells. *Journal of The Electrochemical Society* **166**, F637-F644, (2019) doi:10.1149/2.1301910jes.

69 Maurya, S., Noh, S., Matanovic, I., Park, E. J., Villarrubia, C. N., Martinez, U., Han, J., Bae, C., Kim, Y. S. Rational design of polyaromatic ionomers for alkaline membrane fuel cells with >1 W cm−2 power density. *Energy & Environmental Science* **11**, 3283-3291, (2018) doi:10.1039/C8EE02192A.

70 Wang, T., Shi, L., Wang, J., Zhao, Y., Setzler, B. P., Rojas-Carbonell, S., Yan, Y. High-Performance Hydroxide Exchange Membrane Fuel Cells through Optimization of Relative Humidity, Backpressure and Catalyst Selection. *Journal of The Electrochemical Society* **166**, F3305-F3310, (2019) doi:10.1149/2.0361907jes.

71 Li, Q., Peng, H., Wang, Y., Xioa, L., Lu, J., Zhuang, L. The Comparability of Pt to Pt-Ru in Catalyzing the Hydrogen Oxidation Reaction for Alkaline Polymer Electrolyte Fuel Cells Operated at 80 °C. *Angewandte Chemie International Edition* **58**, 1442-1446, (2019) doi:10.1002/anie.201812662.

72 Zhang, Y., Parrondo, J., Sankarasubramanian, S. & Ramani, V. Detection of Reactive Oxygen Species in Anion Exchange Membrane Fuel Cells using In Situ Fluorescence Spectroscopy. *ChemSusChem* **10**, 3056-3062, (2017) doi:10.1002/cssc.201700760.

73 Parrondo, J., Wang, Z., Jung, M. S. & Ramani, V. Reactive oxygen species accelerate degradation of anion exchange membranes based on polyphenylene oxide in alkaline environments. *Physical chemistry chemical physics* **18**, 19705-19712, (2016) doi:10.1039/c6cp01978a.

74 Nidheesh, P. V. Heterogeneous Fenton catalysts for the abatement of organic pollutants from aqueous solution: a review. *RSC Advances* **5**, 40552-40577, (2015) doi:10.1039/c5ra02023a.

75 Masa, J., Zhao, A., Xia, W., Muhler, M. & Schuhmann, W. Metal-free catalysts for oxygen reduction in alkaline electrolytes: Influence of the presence of Co, Fe, Mn and Ni inclusions. *Electrochimica Acta* **128**, 271-278, (2014) doi:https://doi.org/10.1016/j.electacta.2013.11.026.

76 Yang, M., Liu, Y., Chen, H., Yang, D. & Li, H. Porous N-Doped Carbon Prepared from Triazine-Based Polypyrrole Network: A Highly Efficient Metal-Free Catalyst for Oxygen Reduction Reaction in Alkaline Electrolytes. *ACS applied materials & interfaces* **8**, 28615-28623, (2016) doi:10.1021/acsami.6b09811.

77 Yang, W., Fellinger, T.-P. & Antonietti, M. Efficient Metal-Free Oxygen Reduction in Alkaline Medium on High-Surface-Area Mesoporous Nitrogen-Doped Carbons Made from Ionic Liquids and Nucleobases. *Journal of the American Chemical Society* **133**, 206-209, (2011) doi:10.1021/ja108039j.

78 Broughton, D. B., Wentworth, R. L. & Laing, M. E. Mechanism of Decomposition of Hydrogen Peroxide Solutions with Manganese Dioxide. II. *Journal of the American Chemical Society* **69**, 744-747, (1947) doi:10.1021/ja01196a004.

79 Rophael, M. W., Petro, N. S. & Khalil, L. B. II — kinetics of the catalytic decomposition of hydrogen peroxide solution by manganese dioxide samples. *Journal of Power Sources* **22**, 149-161, (1988) doi:https://doi.org/10.1016/0378-7753(88)87004-6.

80 Malkhandi, S., Trinh, P., Manohar, A. K., Jayachandrababu, K. C., Kindler, A., Surya Prakash, G. K., Narayanan, S. R. Electrocatalytic Activity of Transition Metal Oxide-Carbon Composites for Oxygen Reduction in Alkaline Batteries and Fuel Cells. *Journal of The Electrochemical Society* **160**, F943-F952, (2013) doi:10.1149/2.109308jes.

81 Poux, T., Napolskiy, F. S., Dintzer, T., Kéranguéven, G., Istomin, S. Y., Tsirlina, G. A., Antipov, E.V., Savinova, E. R. Dual role of carbon in the catalytic layers of perovskite/carbon composites for the electrocatalytic oxygen reduction reaction. *Catalysis Today* **189**, 83-92, (2012) doi:https://doi.org/10.1016/j.cattod.2012.04.046.

82 Kéranguéven, G., Royer, S. & Savinova, E. Synthesis of efficient Vulcan–LaMnO3 perovskite nanocomposite for the oxygen reduction reaction. *Electrochemistry Communications* **50**, 28-31, (2015) doi:https://doi.org/10.1016/j.elecom.2014.10.019.

83 Ryabova, A. S., Bonnefont, A., Zagrebin, P., Poux, T., Paria Sena, R., Hadermann, J., Abakumov, A., Kéranguéven, G., Istomin, S. Y., Antipov, E. V., Tsirlina, G. A., Savinova, E. R. Study of Hydrogen Peroxide Reactions on Manganese Oxides as a Tool To Decode the Oxygen Reduction Reaction Mechanism. *ChemElectroChem* **3**, 1667-1677, (2016) doi:10.1002/celc.201600236.

84 Bonnefont, A., Ryabova, A. S., Schott, T., Kéranguéven, G., Istomin, S. Y., Antipov, E. V., Savinova, E. R Challenges in the understanding oxygen reduction electrocatalysis on transition metal oxides. *Current Opinion in Electrochemistry* **14**, 23-31, (2019) doi:10.1016/j.coelec.2018.09.010.

85 Speck, F. D., Santori, P. G., Jaouen, F. & Cherevko, S. Mechanisms of Manganese Oxide Electrocatalysts Degradation During Oxygen Reduction and Oxygen Evolution Reactions. *The Journal of Physical Chemistry C*, (2019) doi:10.1021/acs.jpcc.9b07751.

86 Quan, W., Jiang, C., Wang, S., Li, Y., Zhang, Z., Tang, Z., Favier, F. New nanocomposite material as supercapacitor electrode prepared via restacking of Ni-Mn LDH and MnO2 nanosheets. *Electrochimica Acta* **247**, 1072-1079, (2017) doi:10.1016/j.electacta.2017.07.010.

87 Ryabova, A. S., Napolskiy, F. S., Poux, T., Istomin, S. Y., Bonnefont, A., Antipin, D. M., Baranchikov, A. Y., Levin, E. E., Abakumov, A., Kéranguéven, G., Antipov, E. V., Tsirlina, G. A., Savinova, E. R. Rationalizing the Influence of the Mn(IV)/Mn(III) Red-Ox Transition on the Electrocatalytic Activity of Manganese Oxides in the Oxygen Reduction Reaction. *Electrochimica Acta* **187**, 161-172, (2016) doi:10.1016/j.electacta.2015.11.012.

88 Cao, X., Wang, N., Wang, L., Mo, C., Xu, Y., Cai, X., Lin, G. A novel non-enzymatic hydrogen peroxide biosensor based on ultralong manganite MnOOH nanowires. *Sensors and Actuators B: Chemical* **147**, 730-734, (2010) doi:10.1016/j.snb.2010.03.087.

89 Gonçalves Biancolli, A. L., Herranz, D., Wang, L., Stehlikova, G., Bance-Soualhi,, R., Ponce-Gonzalez, J., Ocon, P., Ticianelli, E. A., Whelligan, D. K., Varcoe, J. R., Santiago, E. I. ETFE-based anion-exchange membrane ionomer powders for alkaline membrane fuel cells: a first performance comparison of head-group chemistry. *Journal of Materials Chemistry A* **6**, 24330-24341, (2018) doi:10.1039/c8ta08309f.

90 Pourbaix, M. Atlas of Electrochemical Equilibria in Aqueous Solutions *NACE International* (1974).

91 Poux, T., Bonnefont, A., Ryabova, A. Kéranguéven, G., Tsirlina, G. A., Savinova, E. R. Electrocatalysis of hydrogen peroxide reactions on perovskite oxides: experiment versus kinetic modeling. *Physical Chemistry Chemical Physics* **16**, 13595-13600 (2014), doi:10.1039/C4CP00341A.

92 Zhang, X., Li, H., Hou, F., Yang, Y., DOng, H., Liu, N., Wang, Y., Cui, L. Synthesis of highly efficient Mn2O3 catalysts for CO oxidation derived from Mn-MIL-100. *Applied Surface Science* **411**, 27-33, (2017) doi:https://doi.org/10.1016/j.apsusc.2017.03.179.

93 Saputra, E., Muhammad, S., Sun, H., Ang, H-M., Tadé, M. O., Wang, S. Shape-controlled activation of peroxymonosulfate by single crystal α-Mn2O3 for catalytic phenol

degradation in aqueous solution. *Applied Catalysis B: Environmental* **154-155**, 246-251, (2014) doi:https://doi.org/10.1016/j.apcatb.2014.02.026.

94 Qiu, Y., Xu, G-L., Yan, K., Sun, H., Xiao, J., Yang, S., Sun, S-G., Jin, L., Deng, H. Morphology-conserved transformation: synthesis of hierarchical mesoporous nanostructures of Mn2O3 and the nanostructural effects on Li-ion insertion/deinsertion properties. *Journal of Materials Chemistry* **21**, 6346-6353, (2011) doi:10.1039/C1JM00011J.

95 Jaouen, F. & Dodelet, J.-P. O2 Reduction Mechanism on Non-Noble Metal Catalysts for PEM Fuel Cells. Part I: Experimental Rates of O2 Electroreduction, H2O2 Electroreduction, and H2O2 Disproportionation. *The Journal of Physical Chemistry C* **113**, 15422-15432, (2009) doi:10.1021/jp900837e.

96 Muthukrishnan, A., Nabae, Y., Okajima, T. & Ohsaka, T. Kinetic Approach to Investigate the Mechanistic Pathways of Oxygen Reduction Reaction on Fe-Containing N-Doped Carbon Catalysts. *ACS Catalysis* **5**, 5194-5202, (2015) doi:10.1021/acscatal.5b00397.

97 Choi, C. H., Choi, W. S., Kasian, O., Mechler, A. K., Sougrati, M. T., Brüller, S., Strickland, K., Jia, Q., Mukerjee, S., Mayrhofer, K. J. J., Jaouen, F. Unraveling the Nature of Sites Active toward Hydrogen Peroxide Reduction in Fe-N-C Catalysts. *Angewandte Chemie* **56**, 8809-8812, (2017) doi:10.1002/anie.201704356.

98 Shah, S. S. A., Najam, T., Cheng, C., Peng, L., Xiang, R., Zhang, L., Deng, J., Ding, W., Wei, Z. Exploring Fe-Nx for Peroxide Reduction: Template-Free Synthesis of Fe-Nx Traumatized Mesoporous Carbon Nanotubes as an ORR Catalyst in Acidic and Alkaline Solutions. *Chemistry – A European Journal* **24**, 10630-10635, (2018) doi:10.1002/chem.201802453.

99 Ramaswamy, N. & Mukerjee, S. Fundamental Mechanistic Understanding of Electrocatalysis of Oxygen Reduction on Pt and Non-Pt Surfaces: Acid versus Alkaline Media. *Advances in Physical Chemistry* **2012**, 17, (2012) doi:10.1155/2012/491604.

100 Osmieri, L., Escudero-Cid, R., Monteverde Videla, A. H. A., Ocón, P. & Specchia, S. Application of a non-noble Fe-N-C catalyst for oxygen reduction reaction in an alkaline direct ethanol fuel cell. *Renewable Energy* **115**, 226-237, (2018) doi:https://doi.org/10.1016/j.renene.2017.08.062.

101 Ramaswamy, N. & Mukerjee, S. Influence of Inner- and Outer-Sphere Electron Transfer Mechanisms during Electrocatalysis of Oxygen Reduction in Alkaline Media. *The Journal of Physical Chemistry C* **115**, 18015-18026, (2011) doi:10.1021/jp204680p.

102 Peng, X., Omasta, T. J., Magliocca, E., Wang, L., Varcoe, J. R., Mustain, W. E. Nitrogen-doped Carbon–CoOx Nanohybrids: A Precious Metal Free Cathode that Exceeds 1.0 W cm−2 Peak Power and 100 h Life in Anion-Exchange Membrane Fuel Cells. *Angewandte Chemie International Edition* **58**, 1046-1051, (2019) doi:10.1002/anie.201811099.

103 Peng, X., Kashyap, V., Ng, B., Kurungot, S., Wang, L., Varcoe, J. R., Mustain, W. E. High-Performing PGM-Free AEMFC Cathodes from Carbon-Supported Cobalt Ferrite Nanoparticles. *Catalysts* **9**, 264, (2019) doi:10.3390/catal9030264.

104 Yang, Y., Peng, H., Xiong, Y., Li, Q., Lu, J., Xiao, L., DiSalvo, F. J., Zhuang, L., Abruna, H. D. High-Loading Composition-Tolerant Co–Mn Spinel Oxides with Performance beyond 1 W/cm2 in Alkaline Polymer Electrolyte Fuel Cells. *ACS Energy Letters* **4**, 1251-1257, (2019) doi:10.1021/acsenergylett.9b00597.

105 Truong, V. M., Tolchard, J. R., Svendby, J., Manikandan, M., Miller, H. A., Sunde, S., Yang, H., Dekel, D. R., Barnett, A. O. Platinum and Platinum Group Metal-Free Catalysts for Anion Exchange Membrane Fuel Cells. *Energies* **13**, 582 (2020).

106 He, Q., Li, Q., Khene, S., Ren, X., Lopez-Suarez, F. E., Lozano-Castello, D., Bueno-Lopez, A., Wu, G. High-Loading Cobalt Oxide Coupled with Nitrogen-Doped Graphene for Oxygen

Reduction in Anion-Exchange-Membrane Alkaline Fuel Cells. *The Journal of Physical Chemistry C* **117**, 8697-8707, (2013) doi:10.1021/jp401814f.

107 Lee, S. H., Kim, J., Chung, D. Y., Yoo, J. M., Lee, H. S., Kim, M. J., Mun, B. S., Kwon, S. G., Sung, Y-S., Hyeon, T. Design Principle of Fe–N–C Electrocatalysts: How to Optimize Multimodal Porous Structures? *Journal of the American Chemical Society* **141**, 2035-2045 (2019).

108 Sa, Y. J., Seo, D-J., Woo, J., Lim, J. T., Cheon, J. Y., Yang, S. Y., Lee, J. M., Kang, D., Shin, T. J., Shin, H. S., Jeong, H. Y., Kim, C. S., Kim, M. G., Kim, T-Y., Joo, S. H. A General Approach to Preferential Formation of Active Fe–Nx Sites in Fe–N/C Electrocatalysts for Efficient Oxygen Reduction Reaction. *Journal of the American Chemical Society* **138**, 15046-15056, (2016) doi:10.1021/jacs.6b09470.

109 Wang, L., Bellini, M., Miller, H. A. & Varcoe, J. R. A high conductivity ultrathin anion-exchange membrane with 500+ h alkali stability for use in alkaline membrane fuel cells that can achieve 2 W cm−2 at 80 °C. *Journal of Materials Chemistry A* **6**, 15404-15412, (2018) doi:10.1039/C8TA04783A.

110 Ren, H., Wang, Y., Yang, Y., Tang, X., Peng, Y., Peng, H., Xiao, L., Lu, J., Abruna, H. D., Zhuang, L. Fe/N/C Nanotubes with Atomic Fe Sites: A Highly Active Cathode Catalyst for Alkaline Polymer Electrolyte Fuel Cells. *ACS Catalysis* **7**, 6485-6492, (2017) doi:10.1021/acscatal.7b02340.

111 Miller, H. A., Bellini, M., Oberhauser, W., Deng, X., Chen, H., He, Q., Passaponti, M., Innocenti, M., Yang, R., Sun, F., Jiang, Z., Vizza, F. Heat treated carbon supported iron (ii) phthalocyanine oxygen reduction catalysts: elucidation of the structure–activity relationship using X-ray absorption spectroscopy. *Physical Chemistry Chemical Physics* **18**, 33142-33151 (2016).

112 Woo, J., Yang, S. Y., Sa, Y. J., Choi, W-Y., Lee, M-H., Lee, H-W., Shin, T. J., Kim, T-Y., Joo, S. H. Promoting oxygen reduction reaction activity of Fe–N/C electrocatalysts by silica-coating-mediated synthesis for anion-exchange membrane fuel cells. *Chemistry of Materials* **30**, 6684-6701 (2018).

113 Firouzjaie, H. A. & Mustain, W. E. Catalytic Advantages, Challenges, and Priorities in Alkaline Membrane Fuel Cells. **10**, 225-234, (2020) doi:10.1021/acscatal.9b03892.

114 Wang, L., Peng, X., Mustain, W. E. & Varcoe, J. R. Radiation-grafted anion-exchange membranes: the switch from low- to high-density polyethylene leads to remarkably enhanced fuel cell performance. *Energy & Environmental Science* **12**, 1575-1579, (2019) doi:10.1039/c9ee00331b.